REPORT DOCUMENTATION PAGE

Form Approved
OMB No. 0704-0188

1. REPORT DATE *(DD-MM-YYYY)*	2. REPORT TYPE	3. DATES COVERED *(From - To)*
26-02-2003	Final Technical	15-02-2001 to 31-03-2002

4. TITLE AND SUBTITLE
Active Control of Jet Noise

5a. CONTRACT NUMBER

5b. GRANT NUMBER
N00014-01-1-0396

5c. PROGRAM ELEMENT NUMBER

6. AUTHOR(S)
A. Krothapalli

5d. PROJECT NUMBER

5e. TASK NUMBER

5f. WORK UNIT NUMBER

7. PERFORMING ORGANIZATION NAME(S) AND ADDRESS(ES)
Florida State University
118 N. Woodward Ave.
Tallahassee, FL 32306-4166

8. PERFORMING ORGANIZATION REPORT NUMBER
FMRL-03-01

9. SPONSORING/MONITORING AGENCY NAME(S) AND ADDRESS(ES)
Office of Naval Research
100 Alabama St. NW Suite 4R15
Atlanta, GA 30303-3104

10. SPONSOR/MONITOR'S ACRONYM(S)
ONR

11. SPONSORING/MONITORING AGENCY REPORT NUMBER

12. DISTRIBUTION AVAILABILITY STATEMENT
Approved for Public Release, distribution is Unlimited

20030320 041

13. SUPPLEMENTARY NOTE

14. ABSTRACT

A novel high-speed jet noise suppression technique using high-pressure gas microjet injection at the nozzle exit was developed with promising results using the laboratory scale jet. The main jet parameters, the nozzle pressure ratio and the temperature ratio are chosen to correspond with realistic engine operating conditions. Keeping in mind the applicability of the technique to full-scale engines, the microjet mass flow was kept at less than 2% of the primary jet mass flow. The A-weighted spectrum with appropriate scaling to reflect the full-scale nozzle show a 6 dBA reduction in the peak noise radiation direction. An attempt is made during this investigation to develop Active Noise Control methods for cancellation of broadband jet noise. A demonstration of successful control architecture has been accomplished using the colored random noise cancellation. An actuator based on pulsed microjet appears to be most promising for the current application. A specially designed micro valve operating at high pressures and high frequencies was developed and tested successfully. The valve was able to provide a pulsed jet operating at nozzle exit mean pressure of about 45 psia at 2000 Hz.

15. SUBJECT TERMS Jet Noise, microjet, pulsed microjet, active control,

16. SECURITY CLASSIFICATION OF:			17. LIMITATION OF ABSTRACT	18. NUMBER OF PAGES	19a. NAME OF RESPONSIBLE PERSON
a. REPORT	b. ABSTRACT	c. THIS PAGE			19b. TELEPONE NUMBER *(Include area code)*
UU	SAR	SAR	UU	76	

FINAL REPORT

ACTIVE JET NOISE CONTROL

ONR CONTRACT NUMBER

N00014-01-1-0396

Submitted to

Propulsion Research Program
Office of Naval Research
800 North Quincy Street
Arlington, VA 22217-5660

By

Department of Mechanical Engineering
FAMU-FSU College of Engineering
Florida State University
2525 Pottsdamer Street
Tallahassee, FL 32310

Principal Investigator

Anjaneyulu Krothapalli, Ph.D.
Don Fuqua Eminent Scholar and Professor

FEBRUARY 2003

ABSTRACT

A novel high-speed jet noise suppression technique using high-pressure gas microjet injection at the nozzle exit was developed with promising results using the laboratory scale jet. The main jet parameters, the nozzle pressure ratio and the temperature ratio are chosen to correspond with realistic engine operating conditions. Keeping in mind the applicability of the technique to full-scale engines, the microjet mass flow was kept at less than 2% of the primary jet mass flow. The A-weighted spectrum with appropriate scaling to reflect the full-scale nozzle show a 6 dBA reduction in the peak noise radiation direction. An attempt is made during this investigation to develop Active Noise Control methods for cancellation of broadband jet noise. A demonstration of successful control architecture has been accomplished using the colored random noise cancellation. An actuator based on pulsed microjet appears to be most promising for the current application. A specially designed micro valve operating at high pressures and high frequencies was developed and tested successfully. The valve was able to provide a pulsed jet operating at nozzle exit mean pressure of about 45 psia at 2000 Hz.

TABLE OF CONTENTS

---

* *Work carried out under subcontract by Planning Systems Incorporated, Melbourne Controls Group, 1901 S. Harbor City Blvd, Suite 720, Melbourne, FL 32901*

1. INTRODUCTION

This report presents the results of active control techniques used to suppress the far-field noise emanated from jet exhaust of fighter aircraft, such as the F-18 (figure 1), at take-off and landing. This technology was developed with a view that we do not have easy access to the primary sources of sound- the unsteady pressure fluctuations in the jet. Instead an attempt is made to control the acoustic fields generated by the primary sources by the operation of secondary sources. The control will be over the near field of the primary sources such that the far field acoustic power is reduced or that the directivity of the field is substantially altered. Destructive interference has long been appreciated as the source of great character in acoustic fields. "Knowing that two different source distributions can generate the same wave field and one source distribution is under our control, then a simple change in sign makes the primary noise field subject to extinction by the presence of the secondary. Furthermore, even though the source of anti-noise can be of completely different construction to that of the primary field, the silence is, in principle, achievable everywhere outside the source distribution"[*].

Figure 1. F-18 aircraft in flight with visible nozzle exhausts.

Active noise control methods have been successfully applied to attenuate the cabin noise in propeller-driven aircraft. It is to be noted that the cabin noise is highly tonal and their levels decay rapidly with increasing mode number. As a result, a small number of sensors and actuators are required to achieve significant levels (~ 10dB) of

[*] J. E. Fffowcs Williams, "Anti-sound", Proc. R. Soc. Lond. A **395**, 1984, pp. 63-88.

noise reduction in the cabin. More recently, the control of combustion instabilities has received considerable attention because of large amplitude flow oscillation in the combustion chamber can often have very deleterious effects. In these cases an unstable feed back cycle is present, with part of the cycle mediated by pressure oscillations in the combustion chamber. The aim of the active control here is to change the effective behavior of the cycle to achieve stability.

It is important to stress that the active control is most feasible and appropriate at low frequencies, where the near field is extensive. For example, a typical far field microphone signals of a full-scale engine, operating at conditions similar to that of an F-18 engine depicts low frequency components with peak Strouhal number (fD/U; f: frequency, D: Nozzle exit diameter and U: Nozzle exit velocity) being around 0.2. The dominant frequencies are within the range of 100 ~ 1000 Hz. At these relatively low frequencies, conventional passive attenuation schemes involving dissipation of sound energy by porous or microstructured materials become impractical and active cancellation techniques offer for them the best prospect of control. However, the high-compactness ratios (= $\boldsymbol{k}\,\boldsymbol{l}$, *where* $\boldsymbol{k} = f/c$, *f is the frequency and c is the speed of sound and* $\boldsymbol{l}$ *is a typical source size*) of the sources involved require carefully designed actuators and their implementation.

In this work we attempted to inhibit the radiation from the source region by the use of microjet injection using high-pressure air and water. During this period attempts are also made with active noise control scheme using high frequency actuators. One of the technical challenges faced during this investigation was the development of a high frequency actuator with sufficient power to affect the initial jet and resulting acoustic characteristics.

The goal of this effort is to demonstrate 10 dB broadband noise reduction at the maximum noise radiation angle of a high speed supersonic jet operating at conditions similar to that of F-18E/F. Next section describes our technical approach and the results. Next section describes the control system architecture, including the several actuator and sensing systems and the template for the adaptive control scheme.

2. HIGH SPEED JET NOISE SUPPRESSION WITH MICROJET INJECTION

The far field noise of a supersonic jet is comprised of four major noise components[1]. The first is a high frequency, short wavelength field that is coherent in phase, commonly referred to as Mach waves. They have plane phase fronts and are confined to a definite wedge sector and emanate from the region within the first few diameters downstream of the nozzle exit, as can be seen in Figure 2. These are generated by small-scale disturbances (or eddies) that are being convected at supersonic speeds so that they emit Mach waves in the direction defined by a disturbance convection velocity and the atmospheric speed of sound[2,3,4]. Surrounding the jet with a gas stream that has a higher speed of sound eliminates these waves as demonstrated by Oertel and Patz[5] and more recently by Papamoschou[6]. The second field is highly directional, peaking at smaller angles to the jet axis (or larger angles to the inlet axis). This noise field is generated from large-scale instabilities reaching peak amplitudes in the region somewhat upstream of the end of the potential core. These sources of noise are associated with the unsteady flow on a scale that is comparable with the local shear layer width. The spectral intensity of this sound field constitutes two distinct peaks[7]. One is associated with the highly directional Mach waves characterized by high positive pressure peaks in the far-field microphone signal[8]. These Mach waves are of significant strength as compared to those that originate very close to the jet exit as discussed above. This intense radiation is observed to emanate from a region between 5~10 nozzle diameters and is associated with supersonically traveling large-scale coherent regions of vorticity[9] (Figure 1). It is found that the far-field intensity contribution of this source is about 30% of the measured total intensity[7,10]. The sources for the second peak appear to be located much further downstream (10~20 nozzle diameters) and are associated with the unsteady flow generated by the large structures quite similar to that in subsonic jets.

The third noise field is at all angles to the jet axis and at higher frequencies. This sound is generated in precisely the same manner as in subsonic flow by the conventional chaotic turbulence. Recent analysis of experimental data by Tam[11] indeed shows vividly the contributions of the distinct components to the total far field spectrum--that associated

with large-scale motions (inclusive of Mach wave radiation if it exists) and a component to small-scale turbulence.

The fourth noise field is commonly referred to as shock-associated noise and it occurs in non-ideally expanded jets. The far-field noise spectrum associated with this noise source typically consists of discrete peaks, representing the screech tones and a broad peak associated with the shock-associated broadband noise[12].

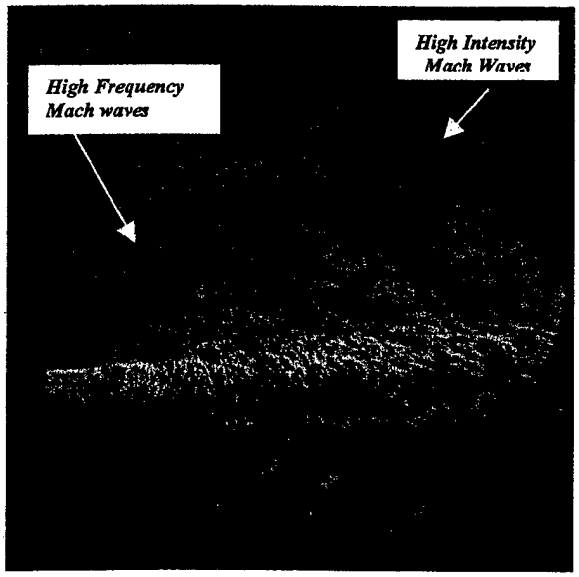

Figure 2. Schlieren picture of a Mach 2 round jet. $T_0 = 1250$ K. $U_j = 1050$ m/s

This section presents a possible approach for the suppression of the dominant large scale mixing noise sources in a supersonic jet. High-pressure microjets are injected into the primary jet at the nozzle exit to manipulate the dominant source region, which extends typically from 5 to 20 diameters from the nozzle exit. Recent results of experiments on an $M_j = 0.9$ round jet suggests that the interaction of the microjets with the jet shear layer reduces the turbulence levels in the noise producing region of the jet[13]. It appears that the microjets influence the mean velocity profiles such that the peak normalized vorticity in the shear layer is significantly reduced and thus inducing an overall stabilizing effect. Therefore, it is suggested that that an alteration in the instability characteristics of the initial shear layer can influence the whole jet exhaust including its noise field.

The present experiments were conducted using a convergent axisymmetric nozzle operating at nozzle pressure ratios of 3, which resulted in jet Mach numbers of 1.38. The nozzle temperature ratio (stagnation temperature/ambient temperature) was kept nominally at 3. The microjet mass flow rate was kept at less than 2% of the main jet mass flow rate.

2. 1 Apparatus, Instrumentation and Procedures

Experiments were conducted in the newly built High Temperature Supersonic Jet Facility at the Fluid Mechanics Research Laboratory of the Florida State University. A schematic of the facility can be seen in Figure 3. A high-displacement reciprocating air compressor, which is capable of supplying air at a maximum storage pressure of 160 bars, drives the facility. Large storage tanks provide a total capacity of 10 m^3. After leaving the storage tanks, the air is subjected to a two-stage pressure control system before it is heated by passing through a Sudden Expansion (SUE) Burner that uses ethylene as the fuel. The burner was originally designed to supply the high Mach number

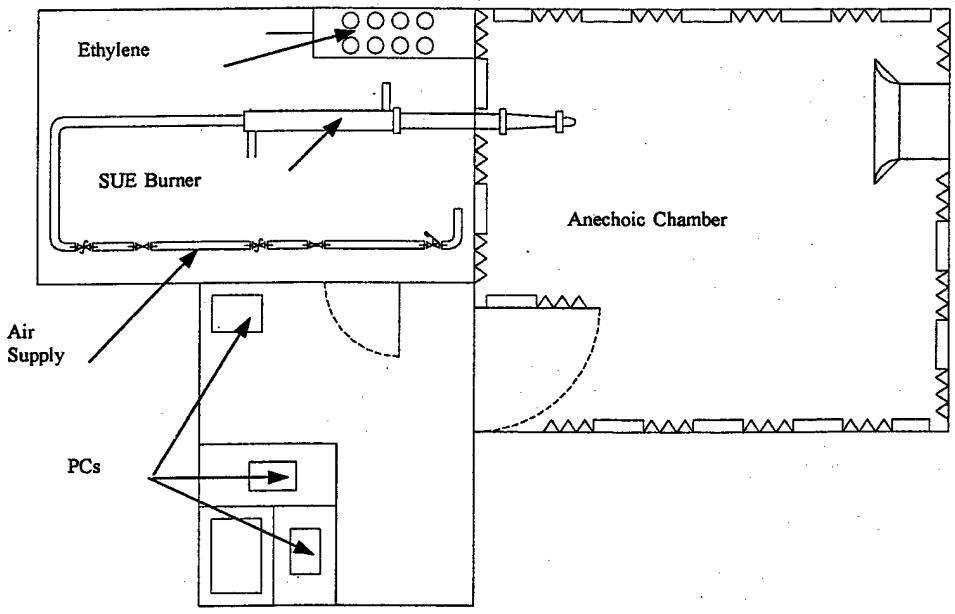

Figure 3. A Schematic of the High Temperature Supersonic Jet Facility.

flow for the testing of ramjet engines. The burner has a simple and reliable construction and it also has wide flame stability limits due to the fact that the fuel injectors are located at the point of expansion. The burner has an inlet diameter of 76.2 mm and an exit diameter of 152.4 mm with an overall length of 0.813 m and it is cooled by a water jacket that surrounds it.

2.1a Flow Management

To minimize the effect of any combustion instabilities on the flow, a 1.525 m long water-cooled pipe having a diameter of 152.4 mm is used. Following the water-cooled extension are three sections: a measurement section, an extension section and a reduction section. Each of them is made of a nickel-based alloy, Nistele 230, which can withstand temperatures in excess of 1400 K without the need for cooling. The conditions of the flow before reaching the nozzle are carefully monitored and managed within these sections.

Immediately following the water-cooled extension is the measurement section. This section is 0.61 m long and has an inside diameter of 152.4 mm. The first 50 mm of this section contains a ceramic honeycomb followed by two titanium screens to suppress any large-scale disturbances in the flow. Midway into the section are four equally spaced ports along the circumference that are 2.54 mm in diameter. Two of the opposing ports are used to measure the static pressure of the airflow. It turns out that at this location the static and stagnation pressures are nearly equal. The other two opposing ports have Omega C-type thermocouples inserted through them so that they can measure the stagnation temperature of the airflow. The extension section follows the measurement section. This section is also 0.61 m long and has an inside diameter of 152.4 mm. Immediately after the extension section is the reduction section. It is 0.61 m long; with it's inside diameter varying linearly from 152.4 mm at its inlet to 76.2 mm at the exit. A nozzle with a 76.2 mm inlet diameter can then be attached directly to the exit of the reduction section. In the present experiments a converging axisymmetric nozzle having an exit diameter of 50.8mm was used. The nozzle upstream of the exit was designed using a fifth-order polynomial with a contraction ratio of approximately 2.25. The stagnation pressure and temperature were held constant to within 0.5% of its nominal value during the experiment.

The jet exhausts into an anechoic chamber that measures 5.2 m wide, 5.8 m long and 4 m high. The walls, ceiling, and floor are covered with high temperature 305 mm deep wedges that were supplied by Eckel Industries, Inc. The wedges are composed of #703 fiberglass and they have a fiberglass cloth covering followed by a mesh covering. There are sections of metal grating covering the wedges on the floor so that personnel movement during experimental setup is possible. The chamber has provisions for adequate ventilation for easy entrainment of the ambient air into the chamber during jet operation. The exhaust system was also treated to minimize any noise generated by the impinging flow. The Inverse Square Law was used to determine the acoustic characteristics of the chamber. The characterization was done with and without the metal grating in place. The cut-off frequency of the chamber is about 500 Hz with the grating in place, while it is about 300 Hz without the grating.

2.1b. Data Acquisition and Automation

There are a number of different conditions that need to be monitored during an experiment in the facility. It is for this reason that an integrated data acquisition and control system was implemented. The system consists of three PCs: the air control PC, the DAQ (data acquisition) PC, and the burner PC. The air control PC uses a LabVIEW-based program to control the air pressure entering the SUE burner. The program also monitors the static pressure and stagnation temperature in the measurement section as well as the ambient pressure, relative humidity, and temperature in the anechoic chamber. All of this data is displayed for easy viewing and is stored for future reference.

The DAQ PC uses a MATLAB-based program to acquire acoustic data. The PC has 3 National Instruments PCI-6110 high-speed data acquisition boards installed in it. Each of the boards can simultaneously sample 4 channels and each channel can be sampled at a rate of 5 MS/s with 12-bit resolution. Each board is then connected to its own National Instruments BNC-2110 connector block. The MATLAB program can be configured to sample any combination of the 12 available channels at any rate up to the maximum. The program also sends a trigger to the LabVIEW program on the air control PC so that all of the relevant conditions are logged.

The burner PC uses a Visual BASIC-based program, supplied by Kaiser Marquardt, to control the SUE burner. It monitors the various pressures, flow rates, and

temperatures of the burner. It also allows for the control of the following solenoid valves located on the burner: main fuel, igniter fuel, spark plug, and nitrogen. This program also controls the main fuel control valve. Due to the importance of this PC it is isolated from the other PCs and it is not a part of any network.

A modern acoustic instrumentation system has been acquired. This instrumentation consists of ten Bruel & Kjaer model 4939 microphones with B&K model 2670 preconditioning amplifiers and three B&K model 2690 Nexus conditioning amplifiers. The signals from the amplifiers are routed through a breakout box that leads to the three BNC-2110 connector blocks mentioned above. Great care was taken to insure that all of the cables from each of the amplifiers to the breakout box and then from the breakout box to the connector blocks were the same length. The microphones were set up in an arc that had a radial distance of 50 diameters from the nozzle exit. The arc covered the polar angle, θ, range from 90 to 150 degrees relative to the jet inlet axis.

Each of the microphones had a relatively flat frequency response up to 100 kHz and was subsequently sampled at 250 kHz. The dataset for each microphone contained 409,600 samples (1.6 sec). This allowed for a fast Fourier transform (FFT) of 4096 points over 100 subsets. Averaging the results for the 100 subsets reduced the random error in the calculation to within 0.1%. The resulting narrowband spectrum had a spectral resolution of 61 Hz.

The overall sound pressure level (OASPL) can be found through the use of two methods. The first method involves integrating under the power spectral density curve to obtain the squared pressure fluctuation and then applying the following well known formula:

$$OASPL = 10\log\frac{p^2}{p_{ref}^2} \qquad (1)$$

where p_{ref} is 20 μPa. The second method uses the pressure data that is obtained from the microphones to compute the root mean square pressure. This value is then squared and then Equation 1 can then be used. In both cases the OASPL value was found to be the same.

A number of corrections must be applied in order to obtain accurate data. The sound pressure level (SPL) at each frequency needs to be determined through the use of

the raw data. The corrections for the actuator response as well as the free-field response are then applied at each frequency. Lastly, the effect of atmospheric absorption at each frequency needs to be determined and applied. This was done through the use of formulas provided by Blackstock[14]. The corrected SPL values are then converted back into pressure values and integration is then performed over the corrected spectrum. The resulting squared pressure value can then be used to obtain the OASPL.

To illustrate the suppression technique on a full-scale engine, the frequencies are divided by a factor of 12 (assuming the full scale nozzle diameter = 0.6 m) and then the frequency spectra are converted into a discrete one-third-octave spectrum. In order to do this, one must first determine the center frequency of each octave band and then its lower and upper limits. The corrected pressure spectrum is then integrated over these limits to determine the SPL value at the respective center frequency. Then the entire spectrum is converted, with the A-weighting to properly reflect subjective judgments of the noise as commonly used in the literature.

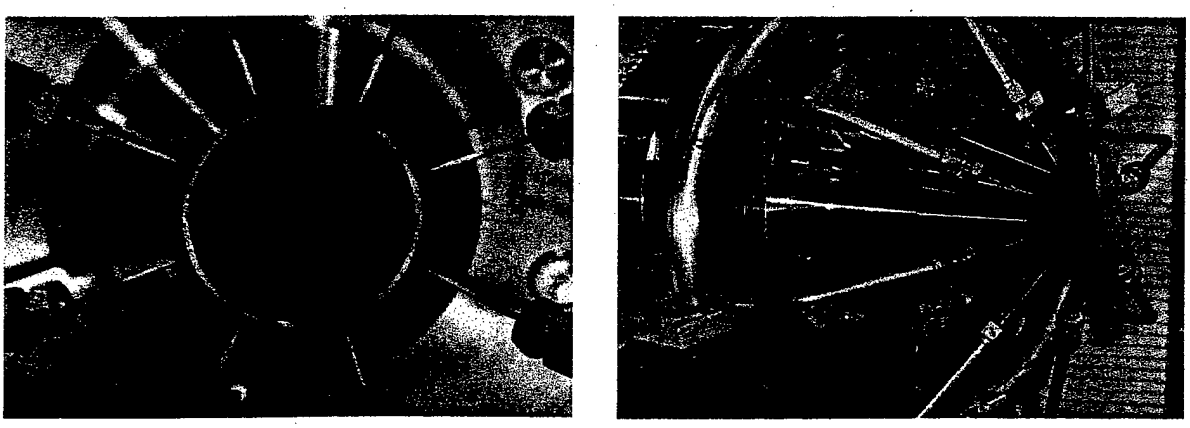

Figure 4. The Microjet Arrangement with Respect to the Primary Nozzle. Primary Nozzle Diameter = 50.8 mm. Microjet Nozzle Diameter = 400 μm.

For the laboratory scale experiments reported here, a converging axisymmetric nozzle with an exit diameter of 50.8 mm was used. The micro-nozzles were made of 400 μm stainless steel tubing. The underexpanded microjets impinge on the shear layer at 6mm downstream of the nozzle exit. The angle of the microjets with respect to the upstream jet centerline was 60 degrees. Typically eight microjets are used, but experiments were also carried out with four and sixteen microjets. The microjet

arrangement is shown in Figure 4. The stagnation pressure of the microjets was varied from 300 psia to 700 psia. At 500 psia, the fully expanded Mach number of the microjet is about 2.91 and the corresponding velocity and Reynolds number of the microjet are 618 m/s and about 8.7×10^3, respectively.

The jet exhausted into a quiet surrounding at ambient conditions. The stagnation temperature of the primary jet was kept at 1033 K. The fully expanded jet velocities for the $M_j = 1.38$ is 760 m/s. The corresponding Reynolds number, based on the nozzle exit diameter, is 4.8×10^5.

2.2. Results and Discussion

Figure 5 shows shadowgraph pictures of the primary jet with and without the microjet injection taken using a high-speed digital camera operating at 1000 frames/sec with an exposure time of 28 μsec. The fully expanded Mach number of the primary jet is 1.38. As expected, a bow shock in front of the microjet appears prominently in the picture on the right. A faint but noticeable trace of the microjet is also visible in the picture. The penetration distance of the microjet is known to be primarily a function of the momentum ratio[15]. For the conditions of the present experiment with $M_j = 1.38$, the correlation[14] gives a value of about 5mm, which is close (~ 6mm) to the measurement from the shadowgraph visualization. The total mass flow rate of the microjets at 500 psia is about 1.1% of the primary jet mass flux.

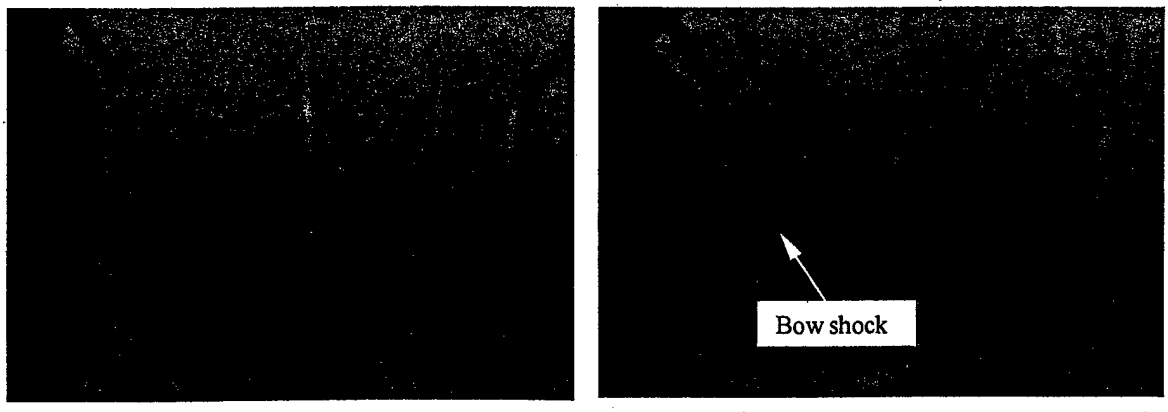

Figure 5. Shadowgraphs of the Jet with and without Microjet Injection. Left: Normal Jet; Right: Air Injection at 500 psia

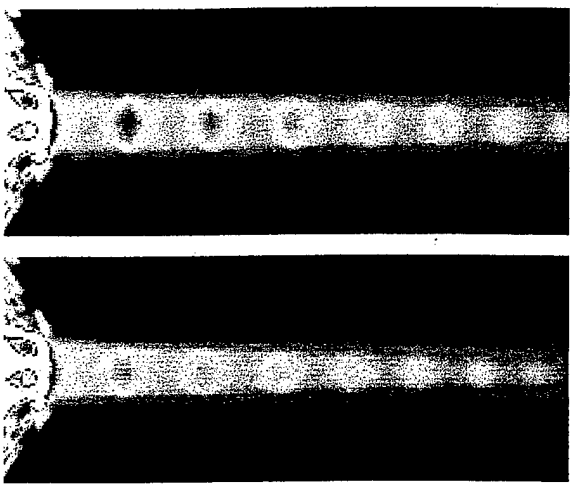

Figure 6. Infrared Pictures of the M_j = 1.38 Jet. Top: Normal Jet; Bottom: Air Injection at 500 psia

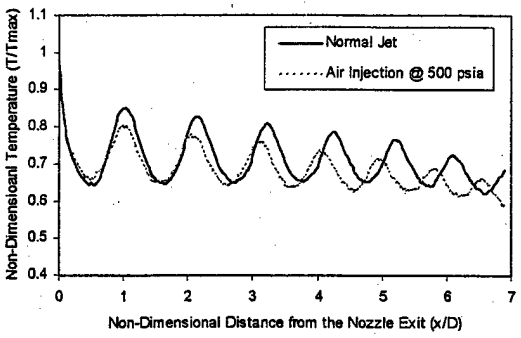

Figure 7. Non-Dimensional Centerline Jet Temperature with and without Microjet

Pictures of the M_j = 1.38 jet taken using an infrared camera with and without the microjets are shown in Figure 6. Due to the underexpanded nature of the jet, several shock cells are seen in the picture. The observed effect of the microjets is to reduce the shock-cell length and the corresponding temperature distribution as shown in Figure 7.

Figure 8 shows the pressure time history of the far-field microphone signal at the peak radiation angle (θ =140°) and at normal to the jet axis for M_j = 1.38. A prominent characteristic of the signal at the peak radiation angle is the random occurrence of distinct bursts of strong narrow positive pressure transients as shown in Figure 9. Such a signal is

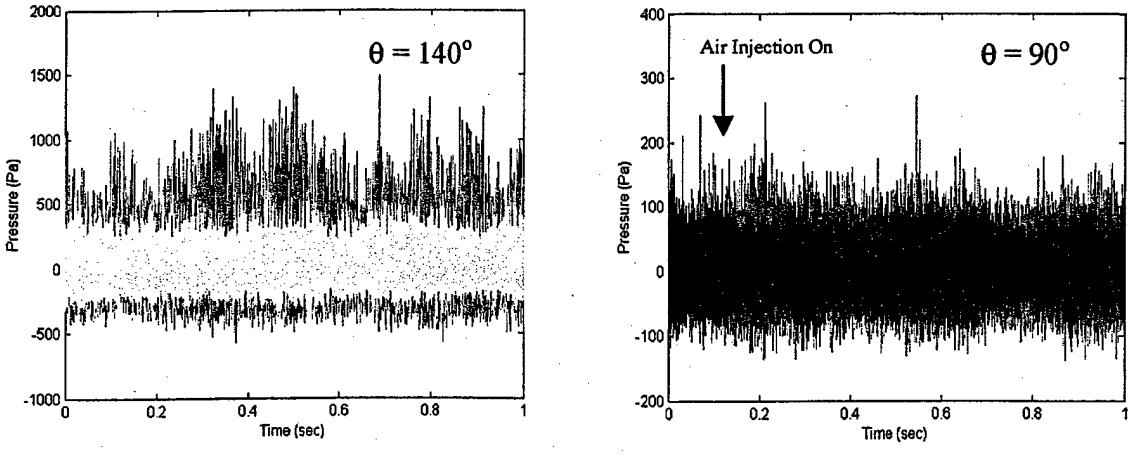

Figure 8. Far-field Microphone Pressure Time Signals for a Normal Jet (red) with Microjet Injection (blue). Left: Peak Radiation Direction; Right: Normal to the Jet Axis.

representative of a crackling jet, first recognized and described by Ffowcs Williams et al[8]. Crackle levels tend to peak at near the eddy Mach angle given by the following equation[5]:

$$\sin\alpha = \frac{1}{M_c}; M_c = \frac{M_j + 1}{\frac{a_\infty}{a_j} + 1} \qquad (2)$$

where M_j and a_j are the fully expanded Mach number and speed of sound of the primary jet, respectively, a_∞ is the ambient speed of sound and α is measured clockwise from the jet axis. The estimated peak radiation angle, θ, using Equation 2 is 139°, which is in agreement with the present results within the experimental uncertainty. Also, included in Figure 7a is the signal obtained with the microjet injection; the lack of the high amplitude positive peaks with injection is clearly depicted, suggesting crackle suppression. Figure 8b shows the signals taken at 90° with and without the microjet injection. In this particular trace, the instant at which the microjet injection turned on is also noted. The

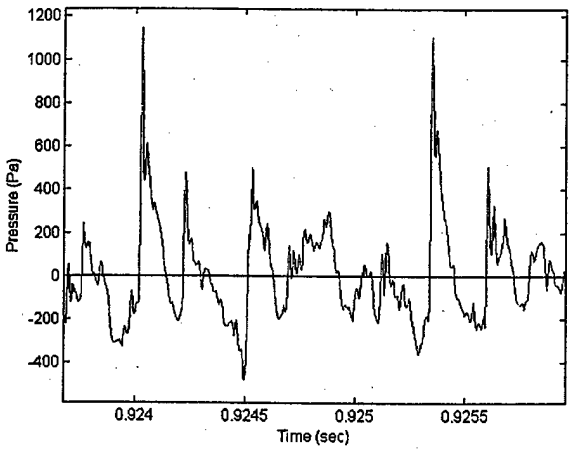

Figure 9. Typical Far-field Microphone Crackle Signal.

relatively low crackle levels found in the signal at this angle of observation are in conformity with the previous observations[8,10]. The effect of microjets on the signal at normal to the jet axis is mostly reflected in the reductions of the overall signal strength.

Ffowcs Williams et al[8] have suggested that the skewness factor of the recorded signal is an effective direct measure of crackle. Keeping this in mind, the skewness of the far field microphone signal at different angles with and without microjet injection is shown in Figure 10. The skewness for jets peaks near the peak radiation angle when the eddy Mach number, M_c, is greater than 1.2. Away from the peak radiation angle, the skewness drops rapidly, an indicator of the absence of crackle. Indeed, the signal at 90°, shown in Figure 7b, confirms this finding. The skewness values, and their dependence on the angular position found in the present experiment, are in general agreement with those of Ffowcs Williams et al[8]. In support of the earlier observation, with respect to the pressure time signals, the crackle suppression in the aft quadrant of the jet exhaust is quite evident by skewness reductions. The energy contained in the spikes responsible for crackle is about 30% of the total energy[7,10], as such it is expected that the OASPL in the peak radiation angle direction be reduced by at least 1.5 dB.

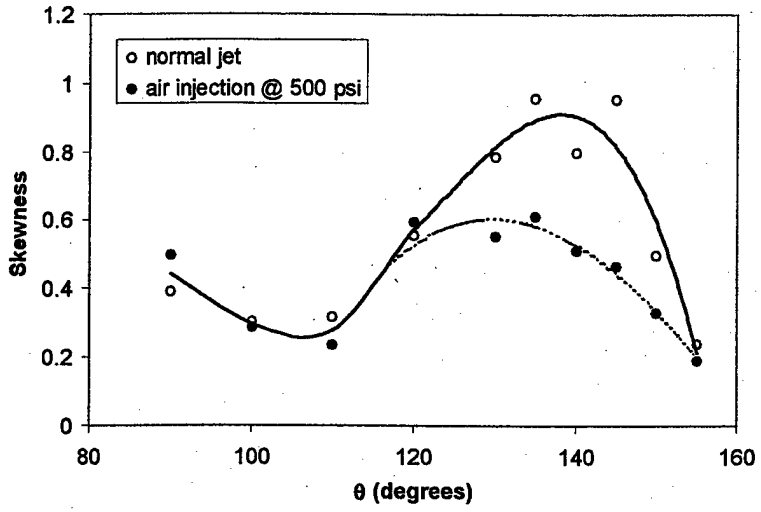

Figure 10. The Directional Distribution of the Skewness Factor with and without Microjet Injection. $M_j = 1.38$.

Figure 11 shows the variation of the OASPL with θ for the normal jet and with microjet injection. Significant reductions in the aft quadrant are observed. At the peak radiation angle, the reduction amounts to about 4.5 dB. Since, crackle is known to contribute only about 1.5 dB, the additional reductions in the OASPL can be attributed to suppression of part of the unsteady flow generated by the large structures, commonly

refereed to as large-scale mixing noise. Measurements taken at $M_j = 0.9$ jet, discussed later suggests that the large-scale mixing noise is also suppressed to some extent by the microjet injection.

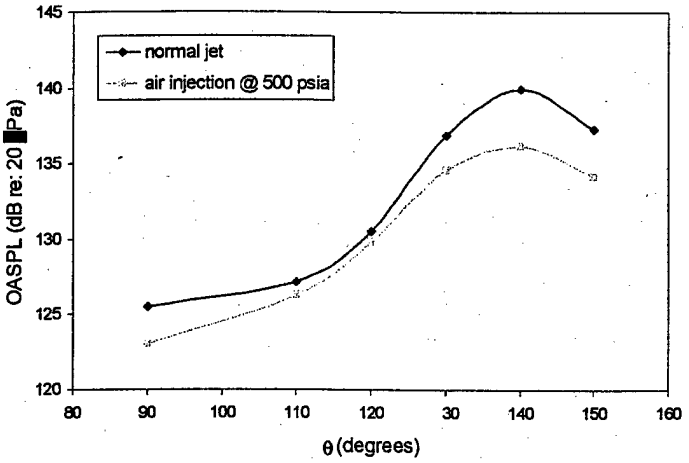

Figure 11. Far-field Directivity of $M_j = 1.38$ with and without Microjet Injection. Nozzle Temperature Ratio = 3.

Spectral measures of the microphone signals show the frequencies affected by the microjet injection and thereby lead to some observations about the influenced source types. The spectrum of a sharp-edged spike shown in figure 8 is flat and evenly distributed over a wide range of frequencies. Hence, the crackle suppression should lead to reductions in a wide band of frequencies in the spectrum. Figure 12 shows the narrow band ($\Delta f = 61$ Hz) frequency spectra corresponding to the far-field microphone signals shown in Figure 8. Although, the computed spectra extends up to 100 kHz, for compactness only the data up to 60 kHz is shown here. Screech tones that are commonly present in underexpanded are clearly seen in the spectra with its fundamental tone being at 3662 Hz. The corresponding Strouhal number ($St = fD_j/U_j$) of 0.26 is in agreement with previous measurements reported in the literature[16]. The suppression of screech tones due to microjet injection is clearly evident. But more importantly, at peak radiation angle, the SPL reductions are observed in the entire spectrum (Figure 12a). Except for the absence of screech tones, the spectrum in Figure 12b, corresponding to $\theta = 90°$, shows little change with microjet injection. Since, the conventional fine and intermediate scale

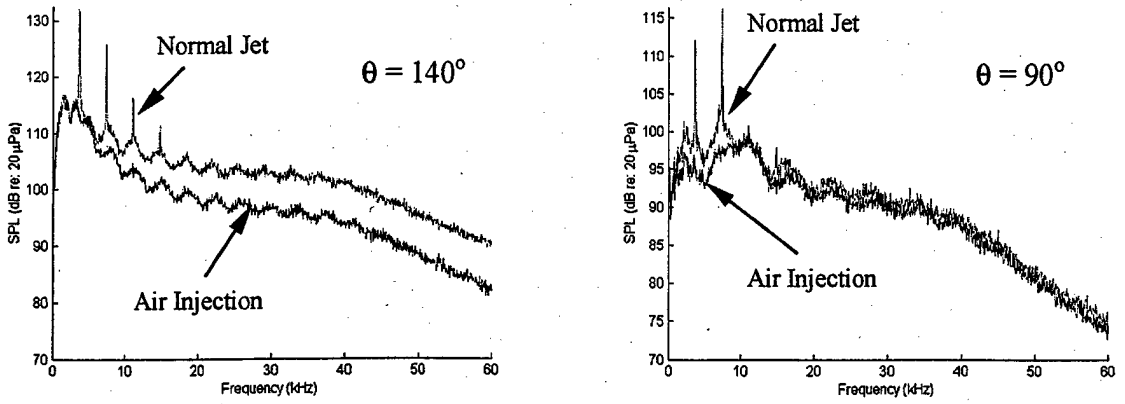

Figure 12. Narrowband Frequency Spectra for the $M_j = 1.38$ Jet. Left: Peak Radiation Angle; Right: Normal to the Jet Axis.

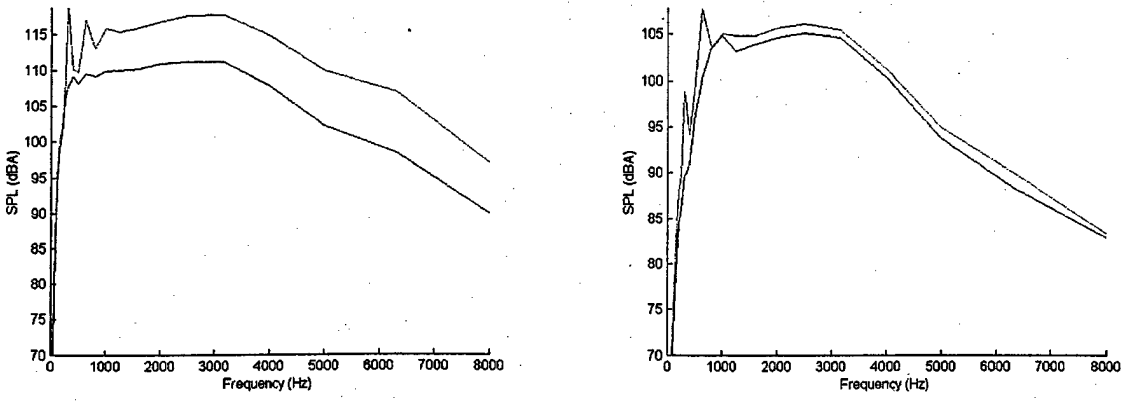

Figure 13. A-weighted Spectra Extrapolated to the Full Scale Corresponding to Figure 11.

chaotic turbulence contributes mostly to the noise at this angle, it is suggested that the microjets have little influence on this component of the noise. Additionally, the broadband shock-associated noise that is dominant in the forward quadrant and at 90o is also minimally affected. From these observations, it is evident that the microjet injection influences the crackle and the large-scale mixing noise. The source of low amplitude undulations seen in the spectra is currently being investigated, but they seem to have little influence on the OASPL based on the agreement of the present data with that of Tanna et al[17].

Using the scaling factor of 12 to account for the full-scale nozzle and the human response to noise, the narrowband spectra are recalculated to yield A-weighted spectra.

Shown in this fashion in Figure 13, at the peak radiation angle, the SPL reductions are quite significant (almost 10 dBA) except at very low frequencies (less than 500 Hz). The corresponding reduction in the OASPL is about 6 dBA. The reduction of 1.5 dBA in the OASPL at $\theta = 90^{\circ}$ may mainly be due to the screech elimination.

3. ACTIVE NOISE CONTROL ARCHITECTURE

3.1. Introduction

The control system addressed in this project addresses the active quieting of jet noise as shown below in Figure 14. The developments of the program documented herein were designed to address the emanated noise by introducing a modulated flow of cold air into the nozzle just prior to exit in such a fashion as to create canceling noise in the far field. Sensors of pressure would be used inside the nozzle to sense incipient fluctuations, and these measured pressure variations would be used, with appropriate adaptive filtering, to drive the modulation actuators to achieve attenuation in the far field. If necessary, a towed array of pressure sensors (microphones) would be used to help characterize and optimize the quieting.

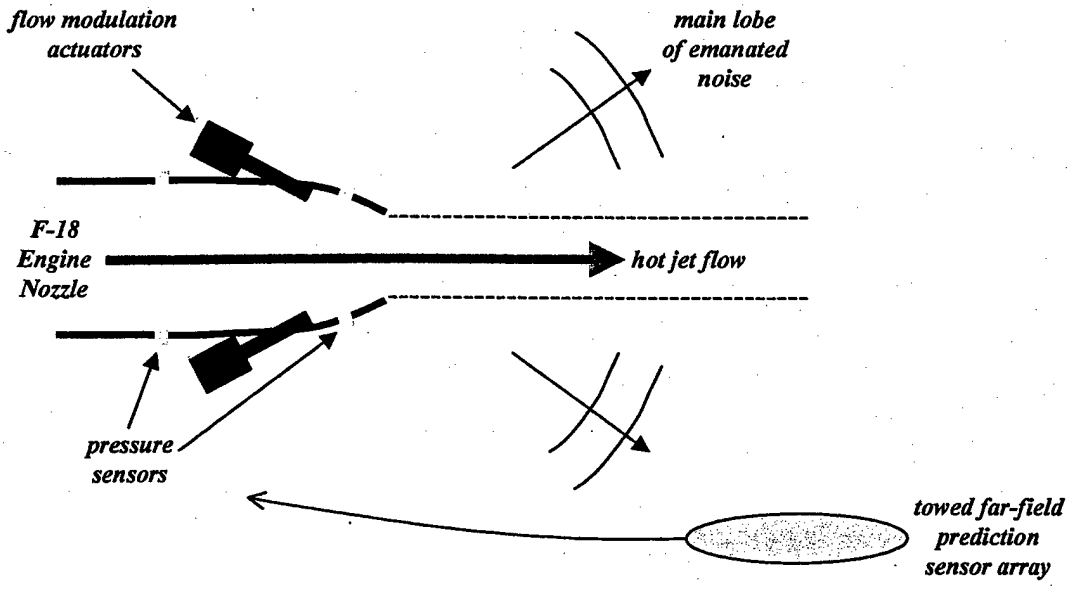

Figure 14. General Control Problem Addressed by the Program

The program had two main thrusts: development and demonstration of a flow-modulation actuator, and implementation and demonstration of an adaptive noise-cancellation algorithm. Actuator development was based on PSI's (Planning Systems Inc.) previously proposed concept of a fast piezo-operated valve. Originally, four

actuators were envisioned. However, when a more thorough investigation of piezo elements was undertaken, it was found that only high-voltage, high-capacitance elements would be capable of the continuous-duty displacements at 1000 Hz. The amplifiers necessary to drive such elements were much more costly than estimated. Further, the difficulty of valve element implementation forced a more step-wise development. Two piezo elements were purchased, with one high-current amplifier. Two separate versions of the actuator were implemented, as will be discussed below. The first of these encountered two main problems which hampered its results:

- The valve elements were not successfully machined by the vendor, causing delays in implementation, excessive leakage and friction and sub-standard friction and closing performance.
- The concept of the actuator caused excessive energy loss, due to the small hole sizes, prior to injection into the hot jet.

However, the first actuator did demonstrate that the piezo element could be successfully integrated to drive the element at full deflection up to 1000 Hz. A revised actuator was manufactured that increased the opening area by a factor of three, and largely resolved the tolerancing and hole mismatching problems. In addition, a small plenum was added after the valve element to reduce the energy loss prior to injection into the main jet. Both low-frequency flow modulation and energy modulation were as designed. However, use of the secondary plenum precluded operation at acoustic frequencies, because the plenum smoothed out and attenuated high-frequency flow variations. A third actuator was then proposed with direct, large-hole modulation via a levered piezo device. However, funding was not available to implement it. The adaptive algorithm was developed and implemented essentially as proposed. However, since no effective actuator was available for testing with the miniature jet, demonstration in PSI's laboratory of the algorithm function was undertaken. Approximately 10 dB of attenuation of a colored noise between 100 and 200 Hz was demonstrated.

The algorithm has the following capabilities:

- Multiple-sensor, multiple-actuator control.
- Feedback, feedforward, or mixed operation.
- Infinite-horizon control optimization.

- No prior or off-line modeling required.

The algorithm was implemented in two major components. The first, which embodied all learning and adaptation, was implemented in Matlab on the host PC. The second, which embodied the real-time control and filtering computations, was implemented C language on a C60 digital signal processor residing on a plug-in card.

3.2 Actuator Description and Demonstration Results

3.2a. Initial Actuator Design

The actuator design was based on a moving valve concept, with the prime mover a piezo element. Previous electromechanical designs have been limited by the need to drive immense currents to achieve the extreme accelerations required by high-frequency operation. Such high currents required complicated cooling systems. Piezo elements have the advantage of the innate ability to achieve extremely large accelerations, albeit over relatively small stroke. Our approach to the valve design was initially fairly conventional, except for the tiny hole sizes required by the small stroke of the piezo element.

Design sizing of the valve opening area followed the analysis by Blondel and Elliott[21]. Design of the actuator centers around a pressurized plenum chamber separated from the source output by a valve. Initially, our design was aimed at achieving a specific mass flow rate modulation of air, without regard to the *energy* of the flow, because we were not aware of the importance of this aspect of the actuator to its modulation capabilities of the jet-engine exhaust. Figure 15 illustrates the design concept. The valve was to be of sufficient size to allow 0.014 kg/sec of air to pass through the valve opening with the plenum chamber pressure set at 620 KPa.

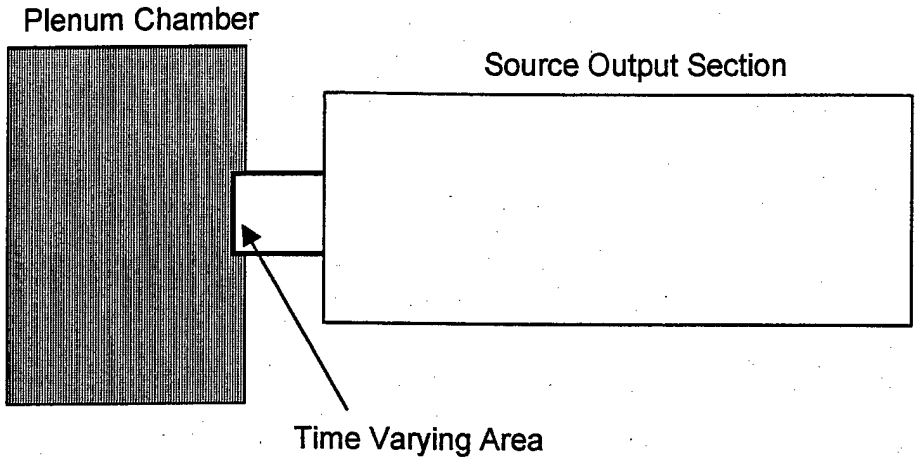

Figure15. Electropneumatic Transducer Concept

From reference 21, using air as the fluid medium, the equation needed to size the orifice for a given set of conditions is:

$$p_2 v_2 = \left(\frac{5}{6}\right)^3 \frac{c_0 p_{pl}}{A_2} A_1 \qquad (3)$$

where:

p_2 = pressure at station 2
v_2 = particle velocity at station 2
c_0 = speed of sound in the medium
p_{pl} = pressure in the plenum chamber
A_1 = time varying area or valve cross sectional area
A_2 = cross sectional area of the output section

Air Valve Size

The cross sectional area needed for the valve was determined as follows. We know for a control volume:

$$\dot{\rho} = A_2 v_2 \rho_2 \qquad (4)$$

where $\dot{\rho}$ is the mass flow rate, A_2 is the cross sectional area of the output section, v_2 is the particle velocity at Station 2, and ρ_2 is the fluid density at Station 2.

So combining the two equations we have:

$$\dot{\rho} = A_2 v_2 \rho_2 = \left(\left(\frac{5}{6} \right)^3 \frac{c_0 p_{pl}}{p_2} A_1 \right) \rho_2 \tag{5}$$

From Boyle's Law:

$$p_2 = \rho_2 R T_2 \tag{7}$$

where p_2 is the pressure at Station 2, R is the universal gas constant, and T_2 is the absolute temperature downstream of the valve. By substituting $\frac{p_2}{\rho_2} = RT_2$ into our equation for $\dot{\rho}$ above and solving for A_1 we get:

$$A_1 = \dot{\rho} \frac{RT_2}{\left(\frac{5}{6} \right)^3 c_o p_{pl}} \tag{8}$$

For our initial test configuration to be tested at the PSI Melbourne laboratory the following values were used to calculate A_1:

$\dot{\rho} = 0.014\ kg/sec$

$R = 287\ Joules/kg^oK$

$T_2 = -40^oC$

$c_o = 340\ meters/sec$

$p_{pl} = 621\ KPa$

From these values we calculated A_1 to be:

$A_1 = 7.75x10^{-6}\ meters^2$ *or* $0.011\ inches^2$

From the cross sectional area we determine the diameter of the valve to be 0.121 inches.

Actuator Drive

Because of the high accelerations associated with opening and closing a valve at up to1000 Hz weight of the moving mass and length of stroke had to be minimized. We could not purchase or develop an actuator capable of opening and closing a 0.121 inch diameter valve at 1000 Hz. Other key issues influencing the choice of a suitable actuator were:

- Small size
- Actuator power requirements
- Survival near a jet nozzle (high Temperatures)
- Self generated heat/survivability
- High accuracy
- Linear dynamic response

A piezo-actuator was chosen as the only suitable means to drive the air vane. The largest piezo-actuator available capable of continuous full stroke operation at 1000 Hz is one with 0.007 inch travel.

Air Valve

A series of 0.007 inch diameter holes were used to realize the cross sectional area of $0.011\,inches^2$ while the valve is open. For an open area of $0.011\,inches^2$ we needed a vane with approximately 292 0.007" diameter through holes. Two concentrically located thin walled stainless steel tubes make up the air vane. To achieve symmetry the vanes were manufactured with 12 rows of 24 holes or 288 holes total. Figure 16 shows the concentric tube air vane. The inner vane is stationary while the piezo-actuator drives the outer vane.

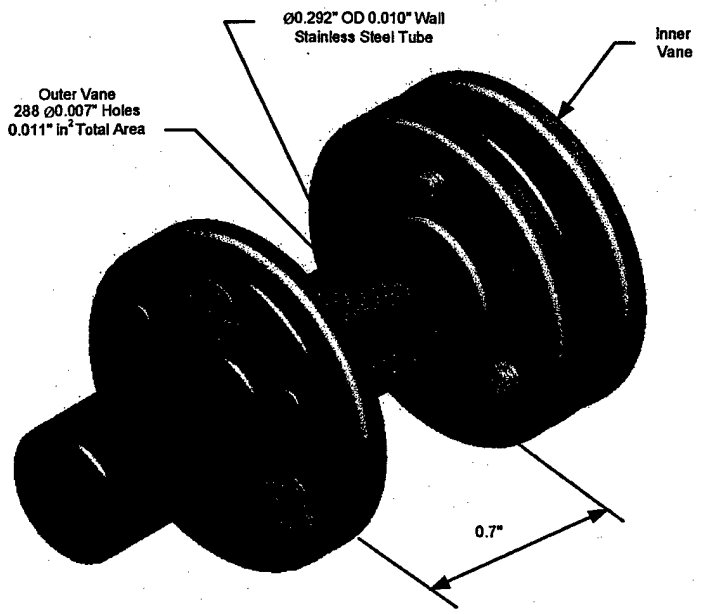

Figure 16. Concentric Tube Air Vane

Flexures

Logarithmic spiral linear flexure bearings were used to position and guide the vane. The flexures were manufactured out of Beryllium Copper 0.010 inches thick. A flexure was attached to each flange of the moving vane to insure linearity of movement. The flexures and positioning hardware are shown in 17 attached to the vanes.

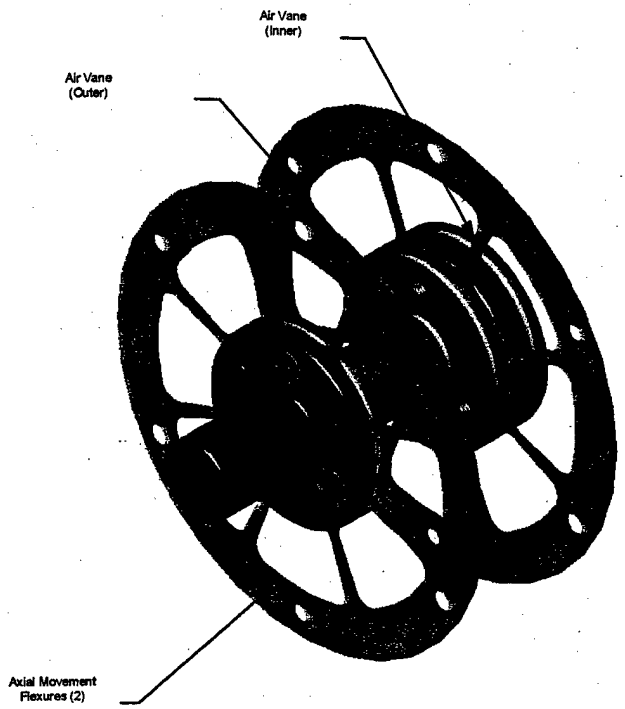

Figure 17. Flexures and Positioning Hardware

Actuator/Air Vane Assembly

The assembled actuator is shown in Figure 18. The piezo-actuator is positioned in-line axially to the air vanes. A moment de-coupling flexure is mounted between the actuator and the vane to eliminate any off axis moments introduced to the piezo-actuator during operation. Off-axis moments can crack the ceramics on the actuator.

Plenum Chamber

Figure 19 shows the plenum chamber with the actuator and associated positioning and spacing brackets assembled. With the actuator assembly mounted inside the plenum chamber a micrometer is placed in series with the inner vane and piezo-actuator to allow adjustment of the vane to a fully closed position prior to modulation. The outer vane is fixed at a known location. With a constant pressure air source the plenum chamber maintains the quasi-static positive air pressure. The end-caps are used to seal the pressure vessel and operate as a base to position the interior components. The plenum chamber is fabricated out of Plexiglas so we can monitor the moving components. The

end-caps are Aluminum. The figure shows the plenum chamber with the actuator and associated positioning and spacing brackets assembled.

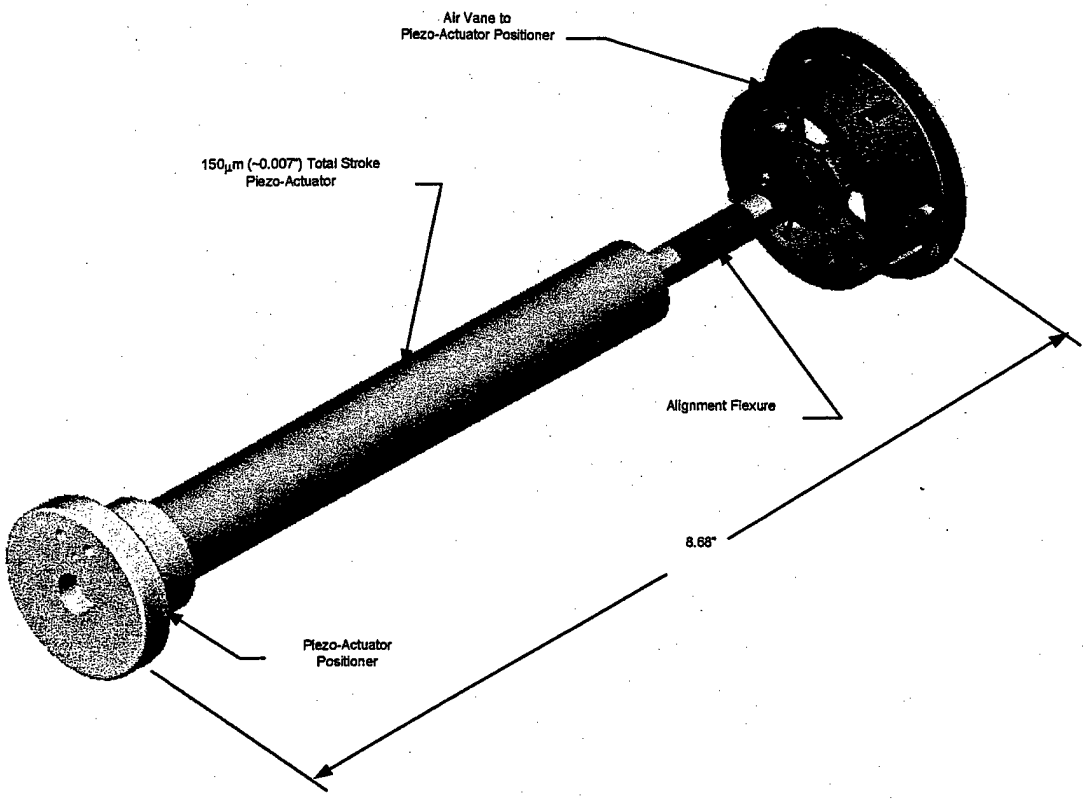

Figure 18. Actuator/Air Vane Assembly

Initial Actuator Test Setup

The actuator test setup is shown in Figure 20. Two Honeywell 4000 pressure transducers were used to measure plenum chamber and downstream pressure. A Piezotronics pressure transducer with a 1 KHz sample rate was also used downstream of the valve. A Flowstream Type 4 OFS flow sensor was used to measure the modulated flow rate. Test results using these sensors in the test setup shown are presented in the following section.

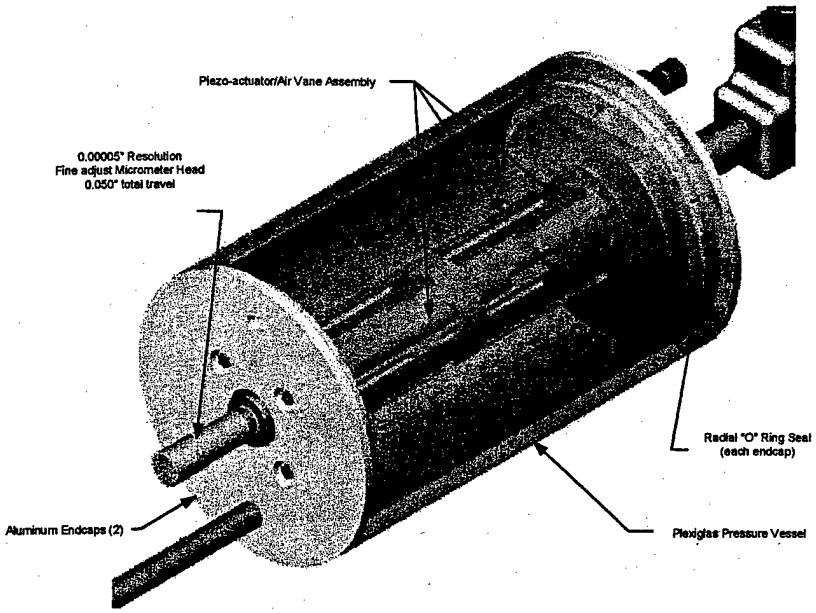

Figure 19. Plenum Chamber with Actuator and Air Vanes

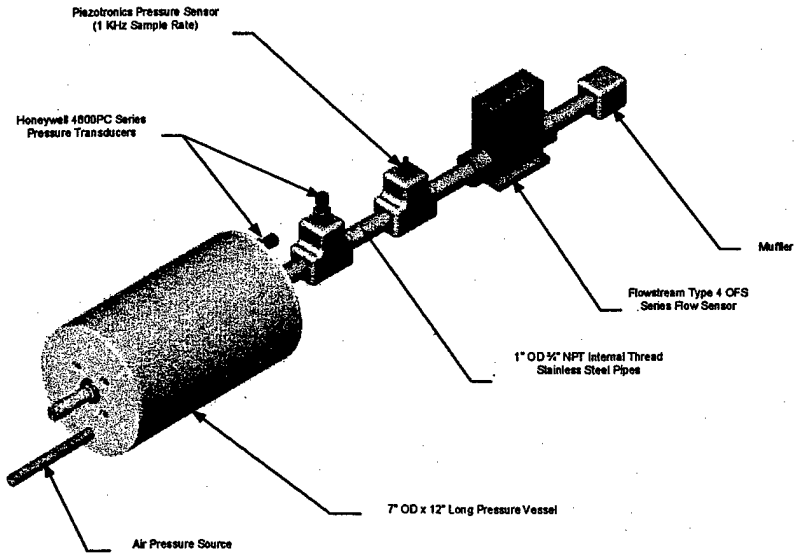

Figure 20. Actuator Test Setup

3.2b. Initial Actuator Test Results

The initial actuator was tested during a 2-day test visit at Dr. Krothapalli's FSU facility. The purpose of the testing was to measure the performance of the actuator when mounted on the jet nozzle. The actuator was attached to the jet nozzle. Cables of several sensors, integral to the actuator, and the piezo element provide interface from the actuator to the data acquisition system. Also, several other FSU-provided sensors, including Kulite pressure sensor (mounted at the jet nozzle), and B&K microphones positioned at the near and far-field, were monitored by the data acquisition system. During the testing, a flow rate sensor was added upstream to the air source of the actuator. This sensor's output was also monitored by the data acquisition system. The Table 1 lists all the test scenarios that were performed.

Table 1 Description of Test Cases and Results for FSU Test Visit

Test Case #	Description of Test Case	Significant Results
	initial actuator checkout	
1 thru 5 (day 1)	Tests performed to determine displacement of actuator's vane. 20, 200, 1000 Hz sine, full voltage drive to piezo, measuring actual applied voltage and position displacment of actuator's vane.	Only getting ±1.4 mils of motion, when expecting ±3.5 mils. Also, motion is highly distorted. We blame binding (rubbing) of inner and outer vane for both problems. Refer to Figure 21for typical vane displacement vs time plot.
	sound pressure testing	
6 and 16	These tests were performed to determine sound pressure due to actuator flow. (with no flow in the jet nozzle) Monitored Kulite pressure and 'nearby' outside microphone (in addition to piezo voltage and vane displacement). Under following conditions: • ambient – no flow, no actuator drive • no flow – actuator set a mid stroke • no flow – actuator driven at 20, 200 and 1000 Hz at full level • 40 psig flow – actuator not driven • 40 psig flow – actuator driven at 20, 200 and 1000 Hz at full level	No difference in sound pressure (at the excitation tone) was measured with and without air flow thru the actuator. This is indicative of the modulated flow rate being much less than expected. Refer to Figure 22 for plots of ambient noise, 20 Hz piezo drive – no actuator flow, and 20 Hz piezo drive – with 40 psi in actuator chamber.
17 thru 20	These tests were performed to determine the sound pressure variation due to actuator flow while there is (cold) flow in the jet. Also, added a data acquisition channel to monitor an upstream (to the actuator) flow rate sensor (in addition to other sensors). • Re-ran some previous tests. • 85 psig flow in actuator. • 44 psig flow thru jet (cold)	Similar results as previous tests. No distinguishable sound pressure variation due to actuator flow output was seen in near-field microphone response.
21 thru 23 (day 2)	Ran several tests to determine if wrapping 'Cerablanket' material around actuator housing would lessen acoustic transmission of noise due to piezo motion.	Measured 86 dB SPL at nearby microphone with and without 'Cerablanket' material. Conclusions: material had no effect on reducing this undesirable noise.

Test Case #	Description of Test Case	Significant Results
24 thru 26	Ran several tests to determine effect of increase air pressure in actuator on flow rate modulation. • 5 Hz, full level drive to piezo • tested 40, 72 and 112 psig (could not get higher pressure due to pressure drop between air tank and actuator, and we're concerned about pressure limitation of actuator)	The mean flow rate increase from 180 to 480 slpm, while the modulated flow rate at 5 Hz increase by factor 5.5 (when increasing 40 to 122 psig actuator inlet pressure). Refer to Figure 23 for PSD of flow rate sensor.
effect of increasing actuator plenum pressure		
27	Added far-field microphone to test set-up. Recorded this and other sensors with • 44 psi cold flow in jet • 122 psi in actuator ***Also, attempted to run 'hot' flow jet, but were unable to light the burners.***	We were able to show fairly good correlation between Kulite pressure and the 'far-field' microphone, which is gives us hope in being able to use the Kulite sensor as feedback in the noise cancellation algorithm. Refer to Figure 24 for correlation result.
actuator flow rate modulation		
	Ran several tests to determine static flow of actuator vs. actuator chamber pressure.	plenum pressure — DC & modulated flow 40 psig — 165 & 20 SLPM 72 psig — 270 & 30 SLPM 122 psig — 450 & 45 SLPM
actuator stagnation pressure		
	Tests were run to determine the stagnation pressure at the outlet of the actuator vs. actuator chamber pressure.	plenum pressure — outlet pressure 40 psig — 0.35 psig 72 psig — 0.875 psig 122 psig — 2.55 psig These tests verified that actuator vane design would not provide outlet pressure needed to modulate far-field sound.

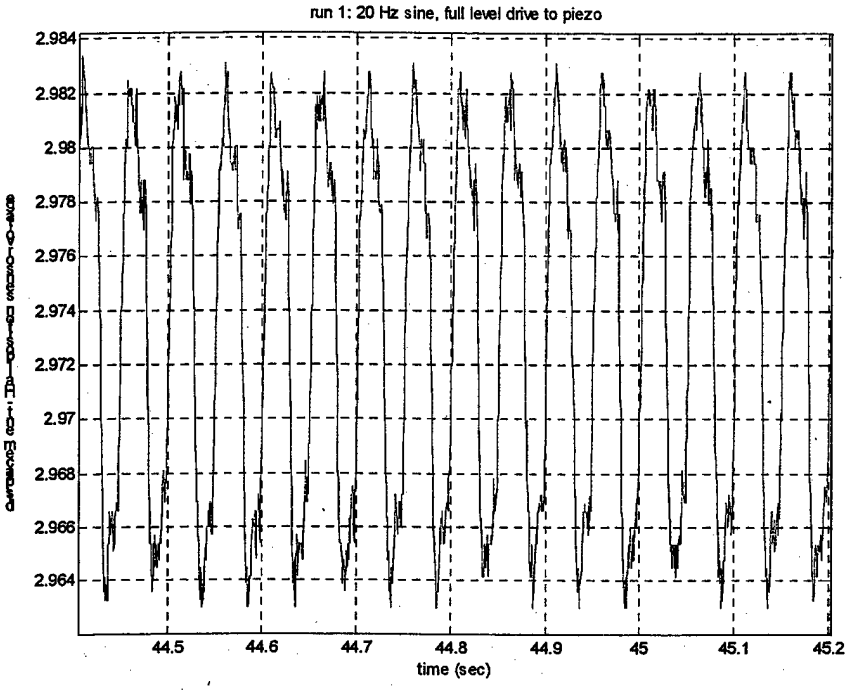

Figure 21. Run 1 - Actuator Vane Displacement vs Time

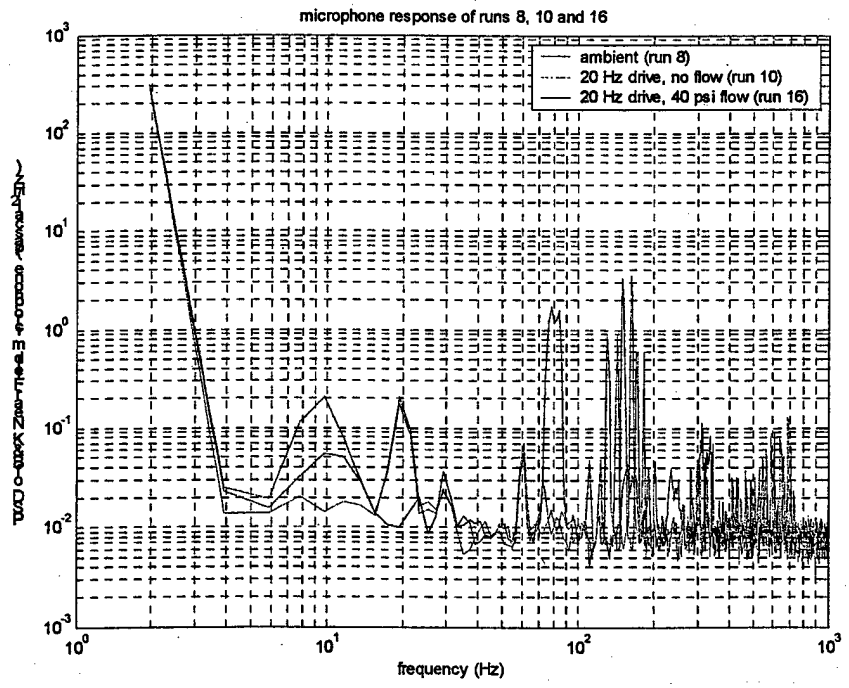

Figure 22. Near-Field Microphone Response to Actuator Output

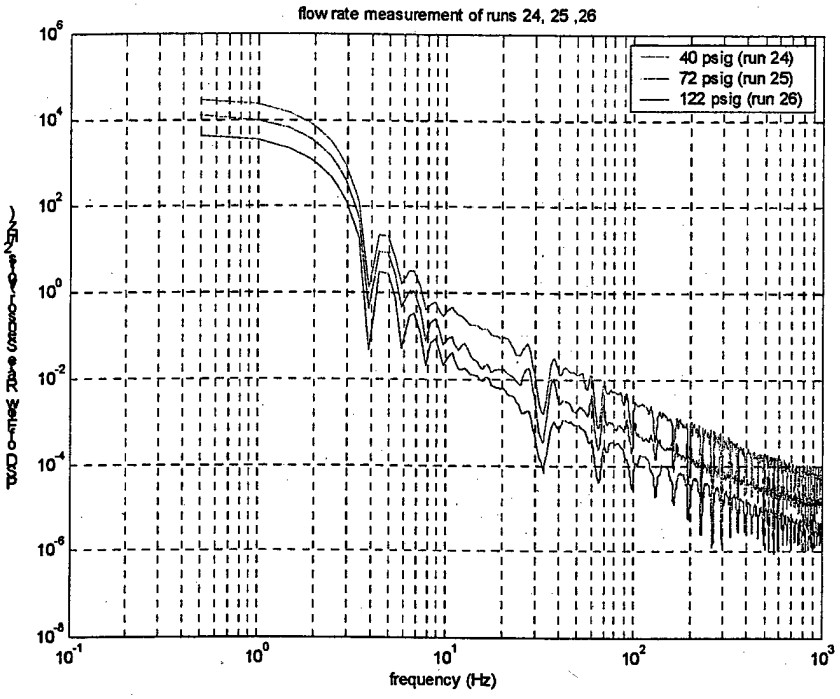

Figure 23. PSD of Flow Rate Sensor for Varying Actuator Inlet Pressure

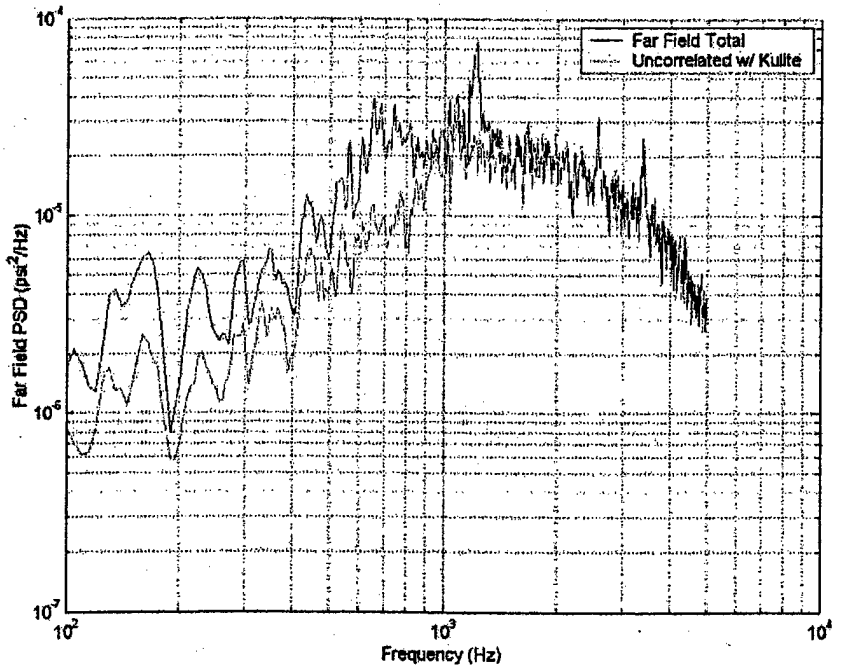

Figure 24. Correlation of Kulite Pressure Transducer to Far-Field Microphone

To address the low flow rate modulation issue, we formulated a plan that would increase it by 5x. This plan included using our improved vane design (with more holes, and fabricated by a higher precision machine shop). From several discussions with Dr. Krothapalli during the final day of the test visit, it was determined that the approach of the initial actuator design was misguided. The actuator requires larger holes (instead of many small ones) that are closer to the flow stream of the jet. The next section describes modifications made to the initial design to incorporate this revised approach.

3.2c. Revised Actuator Design

Results of testing performed on the Initial Actuator proved the cross sectional area of the valve was too small. Irregularities in the fabrication work contributed to the flow rate through the vane being lower than expected. The mass flow rate was approximately 10% of what was needed in a full open position. The new valve design more than tripled the total cross sectional area. The revised vane had 912 0.007 inch holes in 19 rows of 48 holes. The total open area increased from $0.011\,inches^2$ to $0.035\,inches^2$. In addition to increasing the open area, stringent dimensioning and tolerancing methods were used to insure the new vane was fabricated as designed. In addition to changing the open flow area of the vane, we integrated a Stainless Steel plenum chamber to house the actuator. The plenum chamber was designed to interface to the ports on the Florida State University anechoic chamber jet nozzle. A thermal barrier plate was included between the plenum chamber and the nozzle because of the extremely high temperatures on the surface of the nozzle seen during operation. A venturi effect orifice plate was added between the jet nozzle and the thermal barrier plate to magnify the modulation effect of the vane. By introducing this plate between the valve and the source output more energy is transferred to the flow stream. Figure 25 illustrates the new plenum chamber, thermal barrier plate and orifice plate. Figure 26 shows a cross section of the interface plates installed on the FSU jet nozzle.

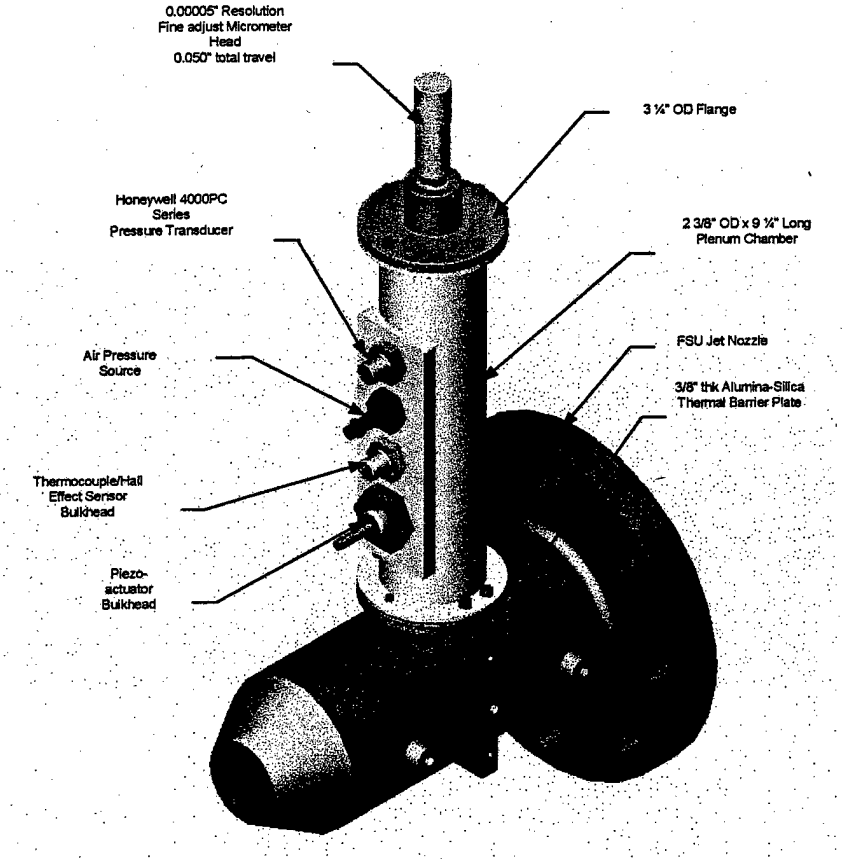

Figure 25. Revised Actuator Plenum Chamber Installed on the FSU Jet Nozzle

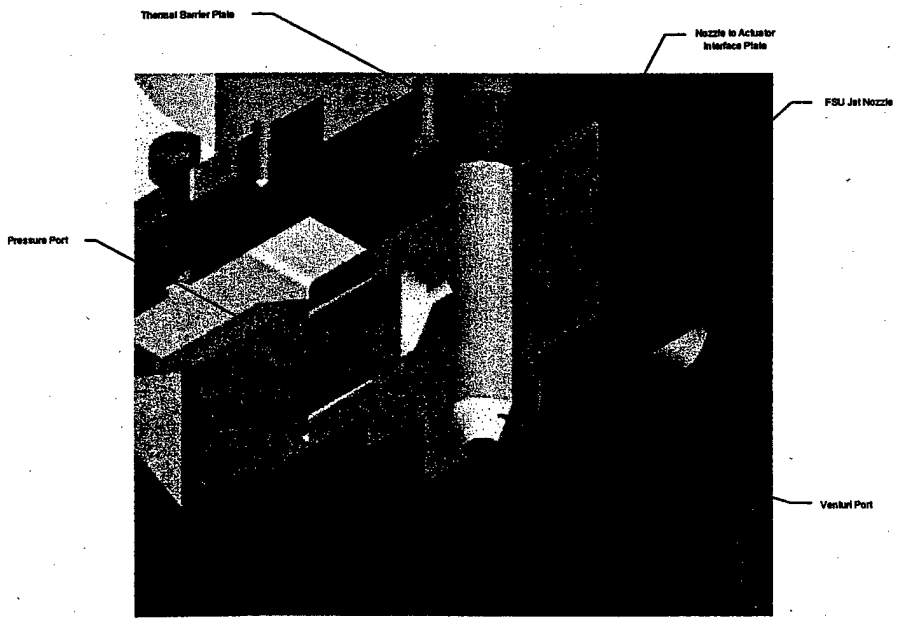

Figure 26. Actuator Interface to Jet Nozzle

3.2d. Revised Actuator Test Results

The final actuator was tested in the lab facilities of PSI's Melbourne, FL office. Unfortunately, several last-minute component failures occurred that prevented testing at the FSU facility. As mentioned previously, the initial actuator design was modified to include an intermediate chamber to increase the outlet pressure. This intermediate chamber and the outlet pressure were measured for various outlet hole sizes, actuator input pressures and actuator drive frequencies. Figure 27 shows the testing configuration. Table 2 below shows the results of various test cases. The inlet pressure was measured with a pressure gauge, the outlet pressure was measured using a pitot tube positioned at the exit of the actuator's intermediate chamber, and the flow rate was measured using an electronic flow meter (Univeral Flow Monitor's model number OFS-MEBS700SLMN-6-A-X7A-D3).

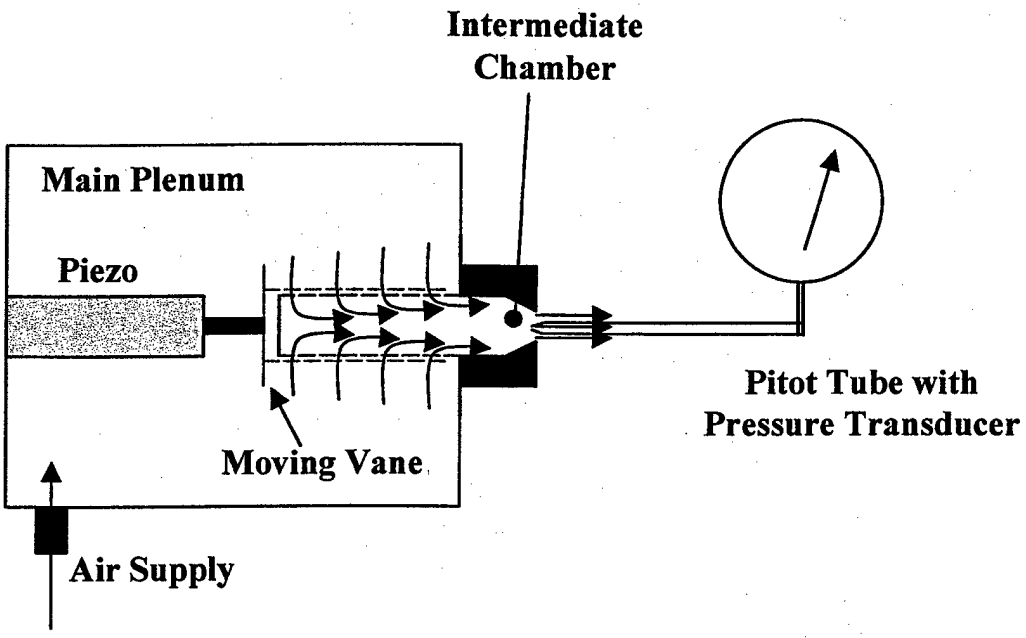

Figure 27. Sketch of Final Actuator Test Configuration

Table 2 Final Actuator Test Cases and Results

Test Case #	Description of Test Case	Results
1	Hole restriction: none Actuator inlet pressure: 40 psig Drive frequency: DC	Actuator Outlet Pressure: Actuator Open: 8.0 psi Actuator Closed: 1.2 psi Actuator Flow Rate: Actuator Open: 510 slpm Actuator Closed: 260 slpm
2	Hole restriction: 1/8" diameter Actuator inlet pressure: 40 psig Drive frequency: DC	Actuator Outlet Pressure Actuator Open: 34.8 psi Actuator Closed: 18.4 psi Actuator Flow Rate: Actuator Open: 350 slpm Actuator Closed: 230 slpm
3	Hole restriction: 1/8" diameter Actuator inlet pressure: 40 psig Drive frequency: 200 Hz 100 Hz 20 Hz 10 Hz	Actuator Outlet Pressure: rms level measure at drive frequency 1.5 psi 2.6 psi 3.0 psi 2.5 psi

These results show that adding the intermediate chamber does produce the desired result of increasing the stagnation (or outlet) pressure. Further testing was disrupted due to failure (cause unknown) of the piezo actuators and amplifier.

3.3. Control Algorithm Description and Results

The control algorithm takes the measured noise signals (from sensors at the engine nozzle exit, in the near field, or in the far-field) and transforms them dynamically to appropriate drive signals for the actuators. Due to the unpredictable and complex nature of the relationship between the actuator signals and the measurements, the control algorithm developed and demonstrated by PSI is adaptive in nature: it constantly measures and updates its model of the system to be controlled and changes the control filtering accordingly.

The control algorithm is based on an architecture used by PSI for several years. The system identification component was previously developed on an SBIR Phase I project for the Air Force Research Lab. The splitting of the implementation of the

algorithm into a PC-host-Matlab component for heavy computations and executive control, and a DSP-target-C component for real-time computation is new to this project. We first describe the control system at the top level, then proceed to more detailed information on the theory and its implementation. A laboratory demonstration of the software and hardware was conducted, and is described last, in Section 0

3.3a. Control Algorithm Top Level Description

The noise control algorithm is a general adaptive control algorithm that is capable of both feedforward and feedback control in MIMO systems. It addresses the control of a system described as shown below in Figure 28. The system is assumed to be linear time invariant, and all quantities are assumed to be vectors in discrete time (i.e., as seen by the control computer). In the figure, the blue boxes represent the external world, and the red, the controller to be designed.

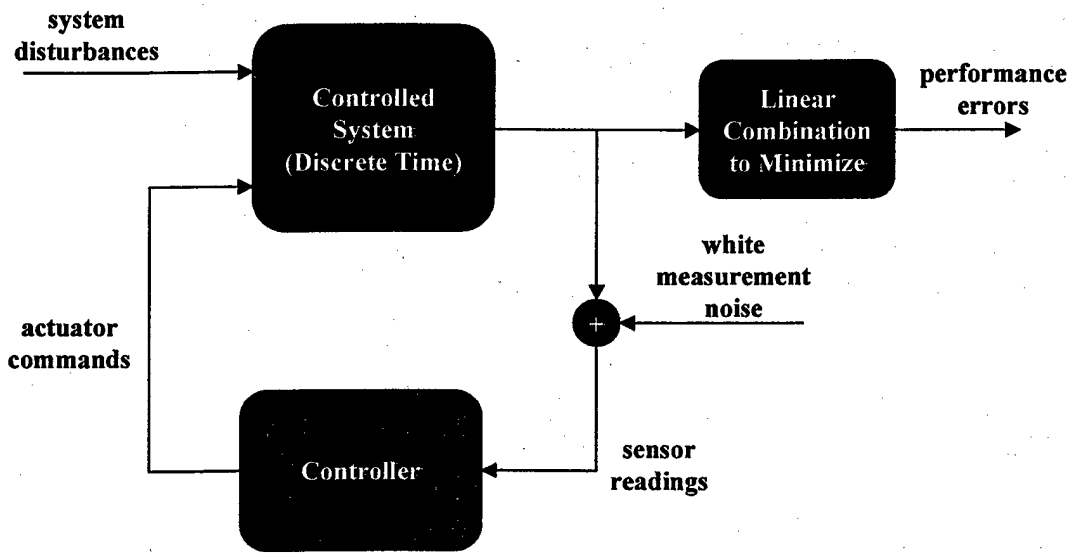

Figure 28. Description of Systems Controllable via the Adaptive Algorithm

System disturbances include all noises (acoustic or otherwise) that drive the system and have significant dynamics (coloring) as seen in the measurements. Actuator commands are the drive outputs sent by the controllers. The controlled system includes the dynamics of the actuators and the sensors in addition to those of the jet engine or other system to be controlled.

The performance errors make up the vector to be minimized by control. For the far-field noise problem, they would ideally be readings of the far-field instantaneous

noise pressure. However, for the adaptive control system they must be accessible signals, such as measurements of perturbations near the exit of the duct, or from a towed microphone array. In the control setup, they are assumed to be a known, linear proportion of one or more of the sensor signals (probably microphones, in the current instance), prior to corruption by additive white noise in the system.

Note that this setup is quite general and includes the possibility of high-gain feedback and feedforward control. Feedforward control emerges naturally when some of the sensor readings are unaffected by the actuator commands, in which case they can be used to help deduce the system disturbances. Note also that by judicious choice of the setup we can feed through some of the actuator signals to the performance errors—effectively causing a tradeoff to be introduced between the level of actuation effort and the other performance errors of the system. This has been implemented in the control system. This setup is precisely that of the classical Linear Quadratic Gaussian (LQG) problem. In fact, we have chosen to use LQG to design the controller adaptively in response to changes in the identified plant, as will be seen in greater detail below. Our adaptive control algorithm (the red block of the previous figure) consists of the principal blocks depicted in Figure 29 below.

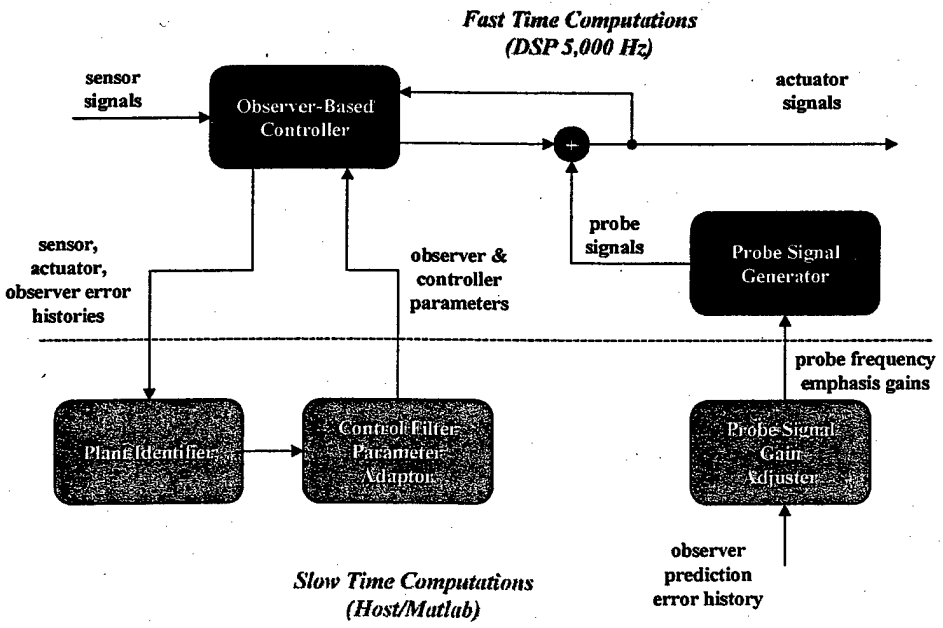

Figure 29. Principal Blocks of the Adaptive Noise Control Algorithm

The computations are split into two major sections: a fast set of computations, which must be completed at the full sample rate of the system, and a slower set, which contains all of the most burdensome calculations associated with learning and adaptation. The fast set is programmed in C code and runs on the target Texas Instruments C60 processor, whereas the slow set is programmed in Matlab, and runs on the host. The setup and implementation of the hardware and communications is discussed further below.

In an ideal system (all dynamics known in advance), no adaptation would be necessary, and the whole system would consist just of the controller itself. The rest of the system is designed to ensure that the correct gains and parameters are used in the controller. We have implemented an observer-based controller. Essentially, this is a real-time, state-space model of the system to be controlled that predicts its behavior and tracks it. It has the form:

$$e(k) = y(k) - c \cdot x(k) \tag{8}$$

$$x(k+1) = a \cdot x(k) + b \cdot u(k) + h \cdot e(k) \tag{9}$$

$$u(k) = f \cdot x(k) + g \cdot e(k) \tag{10}$$

where $x(k)$ is the observer state, $y(k)$ is the set of sensor signals, $e(k)$ is the error in predicting the output, and $u(k)$ is the actuator command vector. The matrices a, b, and c are identified as properties of the system to be controlled, and the gains f, g, and h emerge from the control and observer optimization. The main function of the fast-rate controller is to execute these equations in real time. These equations are an implementation of the optimal LQG control law for the identified system. Further implementation details are provided below in Section 0.

In parallel with the Controller is the Probe Signal Generator. This block puts colored noise into each actuator signal to use as a persistent excitation. Coloring is accomplished by means of a comb filter. The frequency weighting of the noise is calculated in the Probe Signal Gain Adjuster, based on the accuracy of the Controller's predictions of the sensor signals (see(8)) in each frequency band. Once sufficient accuracy is obtained in any band, the probe signal is gradually turned off in that band, eventually turning off entirely and leaving the controller to operate without any disturbance.

The most important block in the operation of the system (other than the Controller itself) is the Plant Identifier. It develops a model of both the effects of the control actuators on the sensor signals and the open-loop disturbance spectra and noises, all in a state-space model form. The algorithm is Larimore's Canonical Variate Analysis method, described further below.

The control optimizer is an ordinary LQG step based on Riccati equation methods using standard Matlab Riccati solvers, with some attention paid to the choices of weighting matrices and the conditioning of inputs. The entire set of software is driven from Matlab. The organization and implementation of the software, and its relationship to the hardware, is described below.

3.3b. Plant Identifier Theory and Implementation

The Plant Identifier (PI) is the key to successful operation of the adaptive controller. If it is successful in characterizing the system to be controlled, then the controller will certainly work. The PI attempts to identify, using only time histories of the actuator commands and sensor signals, the parameters of a model of the system. It uses an implementation of Larimore's Canonical Variate method[21-23] for identifying the parameters of a state-space model, using only time histories of the exogenous inputs and outputs. This implementation is described in the following subsections.

The Problem and Top-Level Solution Description:

The identification problem, in brief, is as follows. Given a set of time histories (possibly distinct windows) of the input vectors $u(k)$ and output vectors $y(k)$, a model is identified of the form:

$$x(k+1) = a \cdot x(k) + b \cdot u(k) + w_1(k) \tag{11}$$

$$y(k) = c \cdot x(k) + d \cdot u(k) + w_2(k) \tag{12}$$

where $x(k)$ is the system state, and $w_1(k)$ and $w_2(k)$ are unknown, zero-mean, inaccessible white noises having covariances $E\left\{w_1(k)w_1(k)^T\right\} = V_1$, $E\left\{w_2(k)w_2(k)^T\right\} = V_2$, and $E\left\{w_1(k)w_2(k)^T\right\} = V_{12}$. The model parameters identified are thus a, b, c, V_1, V_2, and V_{12}. The matrix d may be included or not, depending on whether a feed through term from input to output is postulated for the system or not. The

method works by finding an estimate of the state of the system, and then finding the parameters of the model by least squares estimation, assuming the state is as estimated. The order of the system is chosen by evaluating models of a number of orders and picking the "best" one, using the modified Akaike Information Criterion (AIC)[24,25] as the optimization criterion.

Three essential features of this identification algorithm made it particularly useful for this problem:

1. The algorithm works in the presence of feedback. This is shown, for example, in Ref 22.
2. The method provides an effective means of automatically selecting the model order.
3. The method estimates not only the state-space parameters, but the statistics of the noise as well.

Because the AIC is used for discriminating among various possible models, we briefly digress to describe it's nature qualitatively. Our self-contained development of the theory is reserved for another memo[26]. The AIC is an information-theoretic method for evaluating the nearness of a model to the "true" or operating one. It takes into account both the nearness of the fit of the model to the data and the number of independent parameters that were adjusted to obtain the fit. By "model" is meant, in this context, a probability density function for the observed outputs given the observed inputs. The AIC works for any model in which the history of outputs is a deterministic (nonlinear) function of the inputs and the model parameters, plus an additive Gaussian noise, provided the parameters are estimated using (an approximation to) maximum likelihood estimation (MLE). Recall that in MLE, one selects those values of parameters that maximize the predicted probability for the events actually observed. Numerically, the AIC is the log of the determinant of the best fit error covariance plus twice the number of free parameters (an additional penalization factor is applied to the free parameters for small samples). The absolute level of the AIC is not significant, only relative changes, because we are comparing a number of models in order to choose the best one.

Returning to the ID procedure, there are three basic steps:

Decide on the number of time lags Nlags to use in constructing the estimated state. The state of the system, in keeping with linear Markov assumptions, is assumed to be a linear combination of past inputs and outputs. A practical decision must be made as to how many such past outputs will be considered in the estimation of the state. This is done by fitting a one-step-ahead ARX prediction model to the data using maximum likelihood best fits, and then choosing the number of delays that produces the best-fit according to the AIC. The user must specify an upper bound for the number of possible delays to consider.

Estimate the state history for the system. This is the most difficult part of the problem. According to Markov theory, the state is that vector that is just as useful in predicting the future outputs as is the entire past history of inputs and outputs. The CVA procedure creates a future vector consisting of the Nlags next output values, *with the influence of all present and future input values removed* (present value influence only removed if there's no feedthrough). To remove this future input influence, linear regression is used. The final step is to find the linear combination of past inputs and outputs that best predicts the future vector, for each possible order up to Nlags. This last step is the Canonical Variates procedure, and is accomplished by three singular value decompositions.

Estimate model parameters for each model order and choose the best one. The model parameters are chosen according to least squares, assuming the state consists of the first n elements of the state history vector from the previous step. For example, to estimate the a and b matrices, those values of matrix are chosen that minimize the error in predicting $x(k+1)$ given $x(k)$ and $u(k)$, as can be seen in(11). The residual error is taken as an estimate of the white disturbance vector $w_1(k)$, which is then used to estimate the noise covariances. The best fit error for the model is not, however, just the output covariance estimate V_2, but the (larger) Kalman filter prediction covariance, which depends on all three covariance matrices, as well as the other parameters. This covariance, along with the true number of free stochastic model parameters, is used in the evaluation criterion of AIC. All possible model orders are evaluated, and the best is then

selected (i.e., that minimizing the AIC), and its model parameters recomputed as the final estimates.

These basic steps are elaborated in greater detail below, once we elaborate on another method of Larimore's[27] for saving computations in least squares problems in which successively more regressor variables are to be considered in the fit.

Order-Recursive Linear Least Squares:

Consider the traditional problem of finding the matrix M that minimizes the cost:

$$J = tr\left\{(Y - MX)(Y - MX)^T\right\} \tag{13}$$

In this problem, the columns of the data matrices X and Y might represent time series. Suppose we have a matrix Ψ such that $\Psi^T XX^T \Psi = I_p$, where $p = rank(X)$. Then $X^T \Psi\Psi^T XX^T = X^T$ as can be verified using the compact SVD for X. Expanding the cost we get

$$\begin{aligned} J &= tr\left\{YY^T - MXY^T - YX^T M^T + MXX^T M^T\right\} \\ &= tr\left\{YY^T - MXX^T\Psi\Psi^T XY^T - YX^T\Psi\Psi^T XX^T M^T + MXX^T M^T\right\} \\ &= tr\left\{\begin{matrix} YY^T - YX^T\Psi\Psi^T XX^T\Psi\Psi^T XY^T \\ +YX^T\Psi\Psi^T XX^T\Psi\Psi^T XY^T - MXX^T\Psi\Psi^T XY^T - YX^T\Psi\Psi^T XX^T M^T + MXX^T M^T \end{matrix}\right\} \\ &= tr\left\{Y\left(I - X^T\Psi\Psi^T X\right)Y^T\right\} + tr\left\{\left(M - YX^T\Psi\Psi^T\right)XX^T\left(M - YX^T\Psi\Psi^T\right)^T\right\} \end{aligned} \tag{14}$$

yielding a global minimum of

$$J_{\min} = tr\left\{Y\left(I - X^T\Psi\Psi^T X\right)Y^T\right\} \tag{15}$$

for the choice

$$M_{\min} = YX^T\Psi\Psi^T. \tag{16}$$

Well, suppose we have another set of regressor variables we want to consider in addition to X, Z, and suppose we have, in similar fashion to before, $\Phi^T ZZ^T \Phi = I_q$, where $q = rank\{Z\}$. We need to develop, at minimum expense of computation, a new matrix $\bar{\Psi}$, such that

$$\bar{\Psi}^T \begin{bmatrix} X \\ Z \end{bmatrix} \begin{bmatrix} X^T & Z^T \end{bmatrix} \bar{\Psi} = I_{\bar{p}}, \tag{17}$$

where $\bar{p} = rank\left\{\begin{bmatrix} X \\ Z \end{bmatrix}\right\}$. The new least squares with both variables as regressors is then easy to compute, as before.

The method is as follows. Form the full rectangular SVD

$$\left(\Phi^T Z\right)\left(X^T \Psi\right) = UCV^T \tag{18}$$

where C is a $q \times p$ matrix, and the singular values (diagonal of C) satisfy $0 \le C_{i,i} \le 1$.

This inequality obtains because both $X^T \Psi V$ and $Z^T \Phi U$ are orthogonal matrices, with unit vectors in the columns, so that C represents simply the mutual dot product of these unit columns of the two matrices, and a dot product of unit vectors is the cosine of the angle between them. Next, suppose the number of diagonal elements of C of value less than 1 is r. Form

$$T = \begin{bmatrix} & \begin{bmatrix} \frac{1}{\sqrt{1-C^2_{q-r+1,q-r+1}}} & 0 & 0 \\ 0 & \ddots & 0 \\ 0 & 0 & \frac{1}{\sqrt{1-C^2_{q,q}}} \end{bmatrix} \\ 0_{qx(q-r)} & \end{bmatrix} \tag{19}$$

Note that

$$T\left(I - CC^T\right)T^T = I_r. \tag{20}$$

Finally, set

$$\bar{\Psi} = \begin{bmatrix} \Psi V & -\Psi V C^T T^T \\ 0_{nx p} & \Phi U T^T \end{bmatrix}. \tag{21}$$

We now verify that this matrix satisfies(17):

$$\bar{\Psi}^T\begin{bmatrix}X\\Z\end{bmatrix}\begin{bmatrix}X^T & Z^T\end{bmatrix}\bar{\Psi}=\begin{bmatrix}V^T\Psi^T & 0\\-TCV^T\Psi^T & TU^T\Phi^T\end{bmatrix}\begin{bmatrix}XX^T & XZ^T\\ZX^T & ZZ^T\end{bmatrix}\begin{bmatrix}\Psi V & -\Psi VC^TT^T\\0_{nz\times p} & \Phi UT^T\end{bmatrix}$$

$$=\begin{bmatrix}V^T\Psi^TXX^T & V^T\Psi^TXZ^T\\-TCV^T\Psi^TXX^T+TU\Phi^TZX^T & -TCV^T\Psi^TXZ^T+TU^T\Phi^TZZ^T\end{bmatrix}\begin{bmatrix}\Psi V & -\Psi VC^TT^T\\0_{nz\times p} & \Phi UT^T\end{bmatrix}$$

$$=\begin{bmatrix}V^T\Psi^TXX^T\Psi V & -V^T\Psi^TXX^T\Psi VC^TT^T+V^T\Psi^TXZ^T\Phi UT^T\\-TCV^T\Psi^TXX^T\Psi V+TU^T\Phi^TZX^T\Psi V & \begin{pmatrix}TCV^T\Psi^TXX^T\Psi VC^TT^T-TU^T\Phi^TZX^T\Psi VC^TT^T\\-TCV^T\Psi^TXZ^T\Phi UT^T+TU^T\Phi^TZZ^T\Phi UT^T\end{pmatrix}\end{bmatrix}$$

$$=\begin{bmatrix}I_p & -C^TT^T+C^TT^T\\-TC+TC & \begin{pmatrix}TCC^TT^T-TCC^TT^T\\-TCC^TT^T+TT^T\end{pmatrix}\end{bmatrix}=\begin{bmatrix}I_p & 0\\0 & T\left(I-CC^T\right)T^T\end{bmatrix}=\begin{bmatrix}I_p & 0\\0 & I_r\end{bmatrix}$$

as required.

Intermediate computations are made easier by defining $\hat{X}=\Psi^TX$ and $\hat{\bar{X}}=\bar{\Psi}^T\begin{bmatrix}X\\Z\end{bmatrix}$.

The update is found as follows: $\hat{X}'=V^T\hat{X}$, $\hat{\bar{X}}=\begin{bmatrix}\hat{X}'\\T\left(U\hat{Z}-C\hat{X}'\right)\end{bmatrix}$.

Computations of this type are found in both the first and second major steps of the algorithm.

First ID Step: ARX Model Estimation to Select the Number of Lags:

An ARX model is of the form:

$$y(k)=\sum_{i=1}^{nlags}A_iy(k-i)+\sum_{i=0}^{nlags}B_iu(k-i)+w(k). \tag{22}$$

The second sum starts from an index of 1 if there is no direct feedthrough postulated. The procedure is to compute the residual error from a linear least squares fit of a model having a number of lags specified, and then use the AIC as the indicator of the best model order. The method described in the previous section is used to gradually add more past data to the fit.

Using the notation of the previous section we set:

$$Y=\begin{bmatrix}y(0) & \cdots & y(N-1)\end{bmatrix} \tag{23}$$

$$Z(m)=\begin{bmatrix}y(-m) & \cdots & y(N-m+1)\\u(-m) & \cdots & u(N-m+1)\end{bmatrix} \tag{24}$$

where $Z(m)$ means the Z matrix we're adding to investigate m lags. Note that X is defined recursively:

$$X(m)=\begin{bmatrix} X(m-1) \\ Z(m) \end{bmatrix}, \quad X(0)=\begin{cases} \begin{bmatrix} u(0) & \cdots & u(N) \end{bmatrix} & feedthru \\ empty & else \end{cases} \tag{25}$$

All lag orders up to the maximum specified by the user are examined, and the one giving the least AIC is used.

Second ID Step: State History Estimation:

The state history estimation step is actually comprised of three principal sub-steps: formation of the past history vector, formation of the future history vector, and CVA transformation.

The first sub-step is fairly simple. Considering a time history of N steps beginning with time 0, the past history matrix is:

$$P=\begin{bmatrix} y(-1) & \cdots & y(N-1) \\ \vdots & & \vdots \\ y(-nlags) & \cdots & y(N-nlags) \\ \hline u(-1) & \cdots & u(N-1) \\ \vdots & & \vdots \\ u(-nlags) & \cdots & u(N-nlags) \end{bmatrix}. \tag{26}$$

Column $k \in \{0,1,...,N-1\}$ represents all of the information on which the state $x(k)$ can depend.

The raw future matrix is simply:

$$F_o=\begin{bmatrix} \tilde{y}(0) & \cdots & \tilde{y}(N-1) \end{bmatrix}, \quad \tilde{y}(k)=\begin{bmatrix} y(k) \\ \vdots \\ y(k+nlags-1) \end{bmatrix} \tag{27}$$

in the absence of any external input, this would represent all of the future output information to which the state could have any relevance. In the normal case, when input is presence, this matrix must have removed from it, to the extent possible with the information available, the influence of future inputs. Consider column k of F_o, in the case when no feedthrough is assumed in the plant. The influences of all inputs from $u(k)$ through $u(k+nlags-1)$ must be removed. Because of causality, we know

(without feedthrough) that $y(k)$ can only be affected by $u(k-1)$ and earlier inputs. Ignoring the feedthrough and the stochastic components, we can write:

$$y(k+r)=a^r x(k)+\sum_{m=0}^{r-1} ca^m b\cdot u(k+r-m-1). \tag{28}$$

Define the sensor reading $y(k+r)$ without the previous i inputs (noting causality restrictions) as:

$$\bar{y}(k,r,i)=\begin{cases} y(k+r) & i\le 0 \\ y(k+r)-\sum_{m=0}^{i-1} ca^m b\cdot u(k+r-m-1) & 0<i<r \\ y(k+r)-\sum_{m=0}^{r-1} ca^m b\cdot u(k+r-m-1) & i\ge r \end{cases} \tag{29}$$

The future vector matrix we really want is:

$$F=\left[\hat{y}(0,nlags-1)\ \cdots\ \hat{y}(N-1,nlags-1)\right],\quad \hat{y}(k,i)=\begin{bmatrix} \bar{y}(k,0,i) \\ \vdots \\ \bar{y}(k,r,i) \\ \vdots \\ \bar{y}(k,nlags-1,i) \end{bmatrix} \tag{30}$$

The basic idea is, we start with the raw future vector, which is $\hat{y}(k,0)$, and iterate it forward to $\hat{y}(k,nlags-1)$, which is the desired future vector. The key iteration is:

$$\bar{y}(k,r,i+1)=\bar{y}(k,r,i)-ca^i b\cdot u(k+r-i-1),\quad i<r, \tag{31}$$

which only need by performed on the bottom part of the vector each time (one fewer each iteration). But whence $ca^i b$? Plug in to get the explicit expression:

$$\bar{y}(k,i+1,i)=a^{i+1}x(k)+ca^i b\cdot u(k). \tag{32}$$

We don't have the state—that's the whole idea, after all—but suppose we have some vector $\eta(k)$ containing the state:

$$x(k)=E\eta(k) \tag{33}$$

Then

$$\bar{y}(k,i+1,i)=\begin{bmatrix} ca^i b & a^{i+1}E \end{bmatrix}\begin{bmatrix} u(k) \\ \eta(k) \end{bmatrix}. \tag{34}$$

We could get this matrix by regression, and then just pull out the first nu columns to get $ca^i b$:

$$ca^i b = \left[\bar{y}(0,i+1,i) \quad \cdots \quad \bar{y}(N-1,i+1,i)\right]\begin{bmatrix} u(0) & \cdots & u(N-1) \\ \eta(0) & \cdots & \eta(N-1) \end{bmatrix}^{+}\begin{bmatrix} I_{nu} \\ 0 \end{bmatrix} \tag{35}$$

But notice the product of the last two matrices is independent of i, so we can hold onto it:

$$T = \begin{bmatrix} u(0) & \cdots & u(N-1) \\ \eta(0) & \cdots & \eta(N-1) \end{bmatrix}^{+}\begin{bmatrix} I_{nu} \\ 0 \end{bmatrix}. \tag{36}$$

For the $\eta(k)$ vector we just use the column space basis vector obtained from an SVD of the past matrix from (26).

The summary of the method for obtaining the future vector free of future u is thus:

1. Set up the initial, raw, future matrix as in (27). Compute T as in (36). Set $i=0$
2. Compute $ca^i b$ via (35). Subtract out the influence of $u(k+r-i-1)$ from row $r+1$ of F, for $r=i+1:nlags-1$. Quit if $i=nlags-2$, otherwise increment i and repeat.

The final state estimation step is to perform a CVA relating the past to the future matrix. First we find, via compact (square inner matrix) SVD:

$$P = U_p \Sigma_p V_p^T \tag{37}$$

and similarly for the future vector:

$$F = U_f \Sigma_f V_f^T. \tag{38}$$

Note that, for the purposes of the information present in the time history vectors, the column space bases V_p and V_f are excellent, perfectly conditioned (e.g. $V_p^T V_p = I_p$) substitutes for the originals. The relationship between them is revealed when we compute the full SVD of the dot-product matrix:

$$V_f^T V_p = U_{cva} \Sigma_{cva} V_{cva}^T \tag{39}$$

The state is simply

$$X = V_{cva}^T \cdot V_p^T. \tag{40}$$

This produces a set of states that are independent of one another, related one-to-one with future information vectors, and ordered in descending order of importance.

More can be found on the CVA and its relevance to MLE in Ref. 26.

Third ID Step: Estimate Model Parameters and Pick the Best One

The last step in the ID procedure is fairly simple. The parameters of the model are computed using least squares, for each possible model order up to the size of the system state calculated in the previous step. When there is no feedthrough postulated, two least squares problems emerge. First, the state update equation is used. The state update equation can be assembled as:

$$\begin{bmatrix} x(1) & \cdots & x(N) \end{bmatrix} = \begin{bmatrix} b & a \end{bmatrix} \begin{bmatrix} u(0) & \cdots & u(N-1) \\ x(0) & \cdots & x(N-1) \end{bmatrix} + \begin{bmatrix} w_1(0) & \cdots & w_1(N-1) \end{bmatrix} \tag{41}$$

where the state history and the control input history are given, the a and b matrices are to be estimated, and the noise history $w_1(k)$ is taken as the least-squares fit error. If a model of order n is being estimated, then only the first n state values, as calculated in the previous major step, are included in the fit. The second fit problem uses the measured sensor readings:

$$\begin{bmatrix} y(0) & \cdots & y(N-1) \end{bmatrix} = c \begin{bmatrix} x(0) & \cdots & x(N-1) \end{bmatrix} + \begin{bmatrix} w_2(0) & \cdots & w_2(N-1) \end{bmatrix} \tag{42}$$

where now the noise history $w_2(k)$ is taken as the fit error.

The covariances are estimated via the residuals using simple averaging, e.g.,

$$V_{12} \approx \frac{1}{N} \begin{bmatrix} w_1(0) & \cdots & w_1(N-1) \end{bmatrix} \begin{bmatrix} w_2(0) & \cdots & w_2(N-1) \end{bmatrix}^T. \tag{43}$$

The case of feedthrough is somewhat simpler, because only one, combined, least squares problem arises:

$$\begin{bmatrix} x(1) & \cdots & x(N) \\ y(0) & \cdots & y(N-1) \end{bmatrix} = \begin{bmatrix} b & a \\ d & c \end{bmatrix} \begin{bmatrix} u(0) & \cdots & u(N-1) \\ x(0) & \cdots & x(N-1) \end{bmatrix} + \begin{bmatrix} w_1(0) & \cdots & w_1(N-1) \\ w_2(0) & \cdots & w_2(N-1) \end{bmatrix}. \tag{44}$$

These least squares problems are managed as in the section on re to be considered in the fit.

Order-Recursive Linear Least Squares, so that the inclusion of the next higher order state in the problem has minimal computational impact.

An important subtlety is the assessment of the AIC for each model order. This point is left (intentionally?) vague in Larimore's papers. It seems clear that the simple average fit error V_2 should not be used, because the errors from different steps are not independent,

so that the standard independent trials arguments of MLE do not apply. Instead, the innovations process of the associated Kalman filter, which in the steady state produces independent, identically distributed errors, must be used. This is computed via the Algebraic Riccati Equation (ARE) of Kalman filtering. First, find q to solve:

$$q = a \cdot q \cdot a^T + V_1 - \left(a \cdot q \cdot c^T + V_{12}\right)\left(c \cdot q \cdot c^T + V_2\right)^{-1}\left(a \cdot q \cdot c^T + V_{12}\right)^T \tag{45}$$

Then, the innovations covariance is:

$$\bar{V} = c \cdot q \cdot c^T + V_2 \tag{46}$$

In finding the solution to the ARE, it is necessary to ensure that the states are detectable (stable or observable)—which may not be true numerically if the order is high. Preconditioning is used to ensure both stability and observeability in our implementation. Another method for obtaining $\bar{V}$ would be to run the Kalman filter to get the innovations process, and then use the innovations to obtain essentially the same result as (44). To get the Kalman filter would require the same ARE solution procedure.

The AIC is then computed for each model order as:

$$AIC = N\left(ny\left(1+\log(2\pi)\right)\right) + \log\left(\det\left(\bar{V}\right)\right) + 2f \cdot m \tag{47}$$

where N is the number of output time steps examined, and the number of parameters m is

$$m = \begin{cases} \frac{1}{2}ny(ny+1) + (2ny+nu)n & d \equiv 0 \\ \frac{1}{2}ny(ny+1) + (2ny+nu)n + ny \cdot nu & else \end{cases} \tag{48}$$

The number of states is n, the number of measurements ny, the number of actuation inputs nu. Notice that this number of parameters is far fewer than the number of elements in the matrices of the identified model, because there are a number of free parameters still remaining, which are arbitrary. The number of fixed parameters was derived in Ref. 31. and the stochastic part of this derivation can be also be done by placing the plant in an equivalent Kalman-filter form:

$$x(k+1) = a \cdot x(k) + b \cdot u(k) + h \cdot \bar{w}(k) \tag{49}$$

$$y(k) = c \cdot x(k) + \bar{w}(k), \quad E\left\{\bar{w}(k)\bar{w}(k)^T\right\} = \bar{V}, \tag{50}$$

where the h and $\bar{V}$ matrices are from the Kalman filter computation as before. It can be shown that this rendering of the plant model (not the controller!) has exactly the same statistical behavior (output correlation function) as the original plant model. The total number of parameters is then that of the symmetric $\bar{V}$ $(ny(ny+1)/2)$, of h $(n \cdot ny)$, plus that of the a-b-c realization $(n \cdot (ny+nu))$, keeping in mind the remaining free state basis change allowed, which eliminates n^2 parameters from the bare matrix count.

The factor f provides an extra penalty on the number of parameters when the sample size is small. It is calculated as:

$$f = \frac{N}{N - \frac{m}{ny} - \frac{1}{2} ny(ny+1)}. \tag{51}$$

After selecting the best model order, the parameters (having previously been discarded) are then recalculated, completing the identification process.

3.4. Control Algorithm Theory and Implementation

The control algorithm uses at its core the Linear Quadratic Gaussian theory available since the 1960s[30]. This theory solves the optimum least-squares, steady-state, infinite horizon control problem for a linear time-invariant system. To facilitate discussion, we review the theory results very briefly (to the extent of restating the complete design equations, and adapting them to our implementation), and then proceed to a discussion of some of the practical aspects of the implementation (for example, how do we update the controller on the fly?).

LQG Theory Summary:

Despite the ubiquity of LQG theory, it is remarkably difficult to find a really complete set of design equations written down anywhere. Reference 31 applies to the more difficult problem of designing an optimum order-constrained controller for a higher-order system. However, the equations are easily reduced to the LQG situation as a special case: we present the results of this reduction here. The problem is to minimize, by means of dynamic output feedback compensation applied to the system we described earlier in (11) and (12) (no feedthrough term), the cost functional:

$$J = E\left\{\begin{bmatrix} x(k) \\ u(k) \end{bmatrix}^T \begin{pmatrix} R_1 & R_{12} \\ R_{12}{}^T & R_2 \end{pmatrix} \begin{bmatrix} x(k) \\ u(k) \end{bmatrix}\right\}, \quad \begin{pmatrix} R_1 & R_{12} \\ R_{12}{}^T & R_2 \end{pmatrix} \geq 0 \tag{52}$$

The R_2 penalty is used to control actuator effort, and the coupling matrix R_{12} is zero in most problems. The controller is constrained to be of the form:

$$x_c(k+1) = a_c \cdot x_c(k) + b_c \cdot y(k) \tag{53}$$

$$u(k) = c_c \cdot x_c(k) + d_c \cdot y(k). \tag{54}$$

The design procedure, given these data, is to solve the following two ARE's for positive semi-definite p and q:

$$q = a \cdot q \cdot a^T + V_1 - \left(a \cdot q \cdot c^T + V_{12}\right)\left(c \cdot q \cdot c^T + V_2\right)^{-1}\left(a \cdot q \cdot c^T + V_{12}\right)^T \tag{55}$$

$$p = a^T \cdot p \cdot a + R_1 - \left(a^T \cdot p \cdot b + R_{12}\right)\left(b^T \cdot p \cdot b + R_2\right)^{-1}\left(a^T \cdot p \cdot b + R_{12}\right)^T \tag{56}$$

The optimal matrix values are then:

$$d_c = -\left(b^T \cdot p \cdot b + R_2\right)^{-1}\left(b^T \cdot p \cdot a \cdot q \cdot c^T + R_{12}{}^T \cdot q \cdot c^T + b^T \cdot p \cdot V_{12}\right)\left(c \cdot q \cdot c^T + V_2\right)^{-1} \tag{57}$$

$$b_c = \left(a \cdot q \cdot c^T + V_{12}\right)\left(c \cdot q \cdot c^T + V_2\right)^{-1} + b \cdot d_c \tag{58}$$

$$c_c = -\left(b^T \cdot p \cdot b + R_2\right)^{-1}\left(a^T \cdot p \cdot b + R_{12}\right)^T - d_c \cdot c \tag{59}$$

$$a_c = a + b \cdot d_c \cdot c - b_c \cdot c + b \cdot c_c \tag{60}$$

The dynamic compensation form of (53) and (54) does not bring out the observer that is embedded in the controller, which we need to generate and monitor the modeling error in real time. The observer from we have implemented is developed as follows. Define:

$$h = \left(a \cdot q \cdot c^T + V_{12}\right)\left(c \cdot q \cdot c^T + V_2\right)^{-1} \tag{61}$$

$$f = -\left(b^T \cdot p \cdot b + R_2\right)^{-1}\left(a^T \cdot p \cdot b + R_{12}\right)^T \tag{62}$$

$$g = d_c \tag{63}$$

Then we have:

$$b_c = h + b \cdot g \tag{64}$$

$$c_c = f - g \cdot c \tag{65}$$

$$a_c = a + b \cdot g \cdot c - (h + b \cdot g) \cdot c + b \cdot (f - g \cdot c) = a - b \cdot g \cdot c - h \cdot c + b \cdot f \tag{66}$$

So that

$$u(k) = (f - g \cdot c) x_c(k) + g \cdot y(k) = f \cdot x_c(k) + g\big(y(k) - c \cdot x_c(k)\big) \tag{67}$$

Letting

$$e(k) = y(k) - c \cdot x_c(k) \tag{68}$$

be the output prediction error (i.e., the innovation), the control becomes

$$u(k) = f \cdot x_c(k) + g \cdot e(k). \tag{69}$$

Turning now to the state update,

$$\begin{aligned} x_c(k+1) &= (a - b \cdot g \cdot c - h \cdot c + b \cdot f) x_c(k) + (h + b \cdot g) y(k) \\ &= a \cdot x_c(k) + b\big(f \cdot x_c(k) + g\big(y(k) - c \cdot x_c(k)\big)\big) + h\big(y(k) - c \cdot x_c(k)\big) \\ &= a \cdot x_c(k) + b \cdot u(k) + h \cdot e(k) \end{aligned} \tag{70}$$

so that the state update is just the same as the plant with Kalman observer innovation corrections. The control is plant state estimate feedback with innovation direct feedthrough. This rendering of the control system observer is the method of implementation in the code.

Performance Monitoring and Control Reversion:

It is not unlikely that at some point during the convergence process, the inaccuracies of the identified plant relative to the true system will be such as to cause the optimal controller for the estimated plant to be destabilizing when connected with the true system. To guard against this eventuality, each new controller is tested on a trial basis for a pre-specified amount of time before being accepted as the new baseline. If, during the trial time, the new controller is deemed unacceptable, the real-time system reverts back to the previous baseline. The specific sequence is as follows, once a new controller is available for upload:

1. Compute matrix transformations to transform the state of the baseline controller to that of the new controller, and back again (in case reversion is necessary).
2. Upload the new controller and associated conversion matrices.

3. Calculate the new controller state, start the trial timer, reset the performance monitors, and begin executing the new controller.
4. If the performance monitors detect a fault, map the new controller state back to the baseline controller state, and revert to the baseline (raising appropriate fault flags).
5. If the trial time runs out, without any performance faults, accept the new controller as the baseline and set appropriate flags.

There are three performance monitors that can raise an objection to the new controller: actuator effort, output prediction error, and sensor response. These monitors function by simply filtering the square of each actuator, sensor, or prediction error variable, as follows:

$$q_e(i) = q_e(i) + \delta \cdot \left(e(i)^2 - q_e(i) \right) \tag{71}$$

where $q_e(i)$ is the running average of the i^{th} prediction error. If any of these running averages exceeds the threshold set for it during the trial time, the controller is deemed unacceptable.

It remains for us to clarify how the state of the baseline observer is converted to an "equivalent" state in the new, trial one. We choose that state in the new observer that, given no further control inputs, produces the mean-square closest history of sensor signals to that of the baseline. That is, we choose x_2 to minimize

$$\begin{aligned} J &= \sum_{k=0}^{\infty} \left\| c_1 a_1^{\,k} x_1 - c_2 a_2^{\,k} x_2 \right\|^2 \\ &= x_1^T \left(\sum_{k=0}^{\infty} a_1^{Tk} c_1^T c_1 a_1^{\,k} \right) x_1 - 2 x_1^T \left(\sum_{k=0}^{\infty} a_1^{Tk} c_1^T c_2 a_2^{\,k} \right) x_2 + x_2^T \left(\sum_{k=0}^{\infty} a_2^{Tk} c_2^T c_2 a_2^{\,k} \right) x_2 \end{aligned} \tag{72}$$

Consider the following iteration:

$$\begin{pmatrix} Q_1(k+1) & Q_{12}(k+1) \\ Q_{12}(k+1)^T & Q_2(k+1) \end{pmatrix} = \begin{pmatrix} a_1 & 0 \\ 0 & a_2 \end{pmatrix} \begin{pmatrix} Q_1(k) & Q_{12}(k) \\ Q_{12}(k)^T & Q_2(k) \end{pmatrix} \begin{pmatrix} a_1^T & 0 \\ 0 & a_2^T \end{pmatrix} + \begin{pmatrix} c_1 c_1^T & c_1 c_2^T \\ c_2 c_1^T & c_2 c_2^T \end{pmatrix} \tag{73}$$

with

$$\begin{pmatrix} Q_1(0) & Q_{12}(0) \\ Q_{12}(0)^T & Q_2(0) \end{pmatrix} = \begin{pmatrix} c_1 c_1^T & -c_1 c_2^T \\ -c_2 c_1^T & c_2 c_2^T \end{pmatrix}. \tag{74}$$

It's not hard to verify:

$$Q_1(k) = \sum_{i=0}^{k} a_1^{Ti} c_1^T c_1 a_1^i, \quad Q_{12}(k) = \sum_{i=0}^{k} a_1^{Ti} c_1^T c_2 a_2^i, \quad Q_2(k) = \sum_{i=0}^{k} a_2^{Ti} c_2^T c_2 a_2^i. \tag{75}$$

The solution to the Algebraic Lyapunov Equation produces the limiting sum as $k \to \infty$:

$$\begin{pmatrix} Q_1 & Q_{12} \\ Q_{12}^T & Q_2 \end{pmatrix} = \begin{pmatrix} a_1 & 0 \\ 0 & a_2 \end{pmatrix} \begin{pmatrix} Q_1 & Q_{12} \\ Q_{12}^T & Q_2 \end{pmatrix} \begin{pmatrix} a_1^T & 0 \\ 0 & a_2^T \end{pmatrix} + \begin{pmatrix} c_1 c_1^T & c_1 c_2^T \\ c_2 c_1^T & c_2 c_2^T \end{pmatrix}. \tag{76}$$

Then

$$J = x_1^T Q_1 x_1 - 2 x_1^T Q_{12} x_2 + x_2^T Q_2 x_2. \tag{77}$$

The optimum choice is then found by rearrangement

$$\begin{aligned} J &= x_1^T Q_1 x_1 - x_1^T Q_{12} Q_2^+ Q_2 x_2 - x_2^T Q_2 Q_2^+ Q_{12}^T x_1 + x_2^T Q_2 x_2 \\ &= x_1^T Q_1 x_1 - x_1^T Q_{12} Q_2^+ Q_{12}^T x_1 \\ &\quad + x_1^T Q_{12} Q_2^+ Q_2 Q_2^+ Q_{12}^T x_1 - x_1^T Q_{12} Q_2^+ Q_2 x_2 - x_2^T Q_2 Q_2^+ Q_{12}^T x_1 + x_2^T Q_2 x_2 \\ &= x_1^T \left(Q_1 - Q_{12} Q_2^+ Q_{12}^T \right) x_1 - \left(x_2 - Q_2^+ Q_{12}^T x_1 \right)^T Q_2 \left(x_2 - Q_2^+ Q_{12}^T x_1 \right) \end{aligned} \tag{78}$$

i.e.,

$$x_2 = Q_2^+ Q_{12}^T x_1. \tag{79}$$

So the conversion matrix is $Q_2^+ Q_{12}^T$, and in like fashion, the conversion back is $Q_1^+ Q_{12}$.

Probe Signal Theory and Implementation:

The probe signal is used before proper convergence has been achieved to ensure that sufficiently accurate system identification has occurred for high performance in each sub-band examined.

The probe signal vector is given by:

$$\chi(k) = \sum_{p=p_1}^{p_2} \gamma_p \, \mathrm{Re}\{\theta_p(k)\} \tag{80}$$

where $\chi(k)$ is the probe signal vector, $\theta_p(k)$ is the complex comb filter state for frequency bucket p, γ_p is the real scalar gain to use for frequency bucket p, and p_1 and p_2 are the indices of the first and last frequency buckets to use.

The comb filter state is a running FFT over the last L values of a zero-mean univariate white noise input vector $w(k)$:

$$\theta_p(k)=\begin{cases}\frac{2}{L}\sum_{i=0}^{L-1}w(k-i)e^{j\frac{2\pi}{L}pi} & 1\le p<\frac{L}{2}\\ \frac{1}{L}\sum_{i=0}^{L-1}w(k-i)e^{j\frac{2\pi}{L}pi} & else\end{cases} \tag{81}$$

The factor of two is used for all but the DC and $L/2$ frequency buckets because only positive frequency buckets are included. The updates to $\theta_p(k)$ are computed recursively via:

$$\theta_p(k)=\begin{cases}e^{j\frac{2\pi}{L}p}\cdot\theta_p(k-1)+\frac{2}{L}\left(w(k)-w(k-L)\right) & 1\le p<\frac{L}{2}\\ e^{j\frac{2\pi}{L}p}\cdot\theta_p(k-1)+\frac{1}{L}\left(w(k)-w(k-L)\right) & else\end{cases}. \tag{82}$$

A circular buffer is used to maintain a record of the last L values of the input noise.

The gains γ_p are adjusted as follows:

1. Obtain a set of time data of the output prediction error. Organize the data into windows of length L. Compute the FFT of the data.
2. In each frequency bucket, if any component of the prediction error in the bucket is larger than the reference level for that component, double the probe gain for that bucket. Otherwise, cut the probe gain for that frequency bucket in half.
3. Limit the allowable probe gain level in each frequency bucket to a predetermined amount.
4. Update the gains in the probe output computation.

This completes the probe computation and adjustment theory.

Software and Hardware Implementation:

The control algorithm is implemented using a combination of DSP-based code for fast execution time, and Matlab routines for high flexibility and ease of programming. The block diagram of the hardware implementation is shown below in Figure 30. A Gateway PC Workstation hosts an Innovative Integration M67 DSP board in one of its PCI slots. The DSP board has a Texas Instruments 'C67 digital signal processor, and includes a Servo16 analog I/O module (also supplies by Innovative Integration). The analog signals (both input and output) are filtered using the Krohn-Hite anti-aliasing filtering electronics (corner frequency fixed at 5000 Hz). The filtered actuator command voltage is then routed to the piezo amplifier (RCV 1000/7 made by Piezo-Mechanik of Germany). The (0 to 1000 volt) drive voltage from this amplifier goes to the piezo-actuator (two different model numbers "PSt 1000/10/150 VS25 –HP", and "PSt 1000/10/150 VS25 -HS/HAT" were purchased, also from Piezo-Mechanik, to compare their stroke at high frequency).

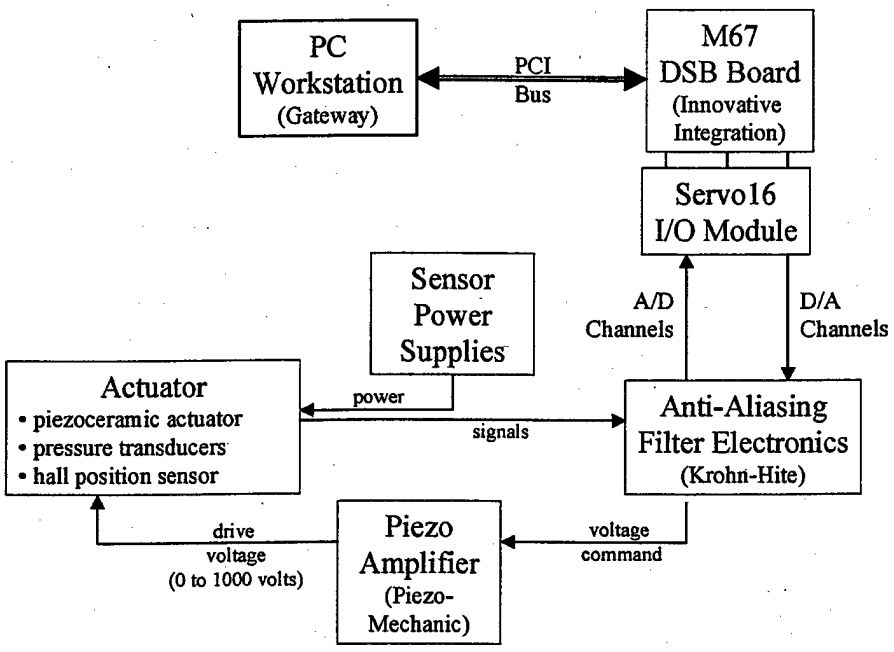

Figure 30. Block Diagram of System Hardware

As mentioned previously, the algorithm was partitioned to executed on both the DSP and the PC, as shown in Figure 31 below. Routines requiring fast execution time, such as data acquisition and controller implementation, were implemented on the DSP.

Routines that could be run in the background, such as identification and control design, were run in Matlab on the PC (this turned out to be huge time saver because it eliminated the conversion of Matlab m-files to c-code). Of course, other routines were necessary to transfer commands and data between the DSP and PC.

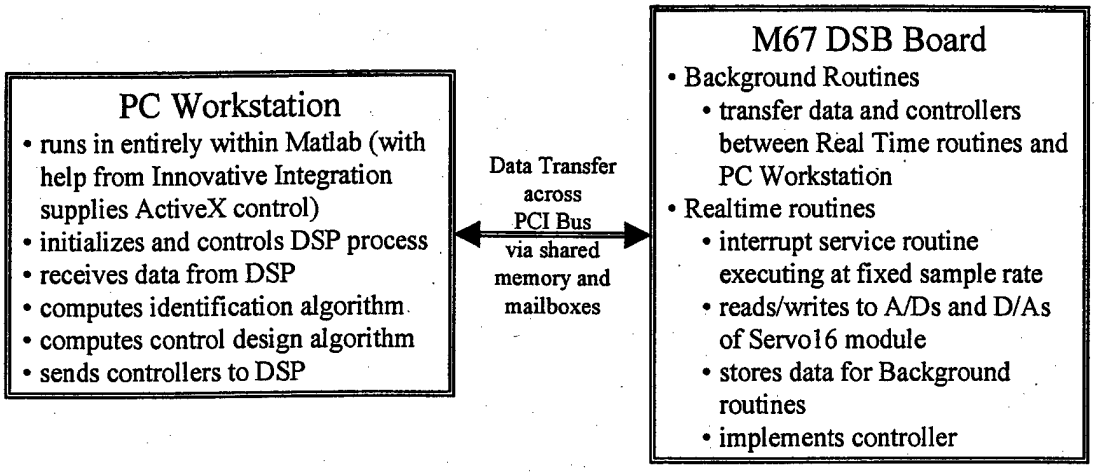

Figure 31. Top Level Software Architecture

The routines of highest interest working on the PC Host in the Matlab environment are described below in Table 3. These files (with the exception of runTarget.m) are in "c:\projects\common mfiles". The top level routines are usually called directly by a program such as "test3.m". In the table, the indented routines are called by the one above ("adaptcontrol.m").

Table 3. Main Matlab m-Files for Control on the Host

Matlab m-File	*Purpose*
runTarget	initializes DSP hardware, starts main shell and interrupts
adaptparams	sets up default parameters for the adaptive controller
adaptcontrol	main routine for adaptive control on host
sendcmd	sends a command to the DSP application
getctlstatus	gets status of the currently operating controller from the DSP
probeadjust	finds new adjusted gains of the probe frequency buckets
sendprobegains	sends the host the new probe gains for immediate implementation
gethistory	gets another time window of data from the DSP of actuator commands, sensor signals, and output prediction errors
cvaid	identifies a new plant model
dlqg	computes the parameters of an LQG controller
stateconvert	computes conversion of states between two controllers
tryobserver	sends a new controller to the DSP for immediate implementation, waits to see whether it worked out

A description of the low-level Matlab m-files and related files for controlling and communicating with the DSP is given in Table 4 below.

Table 4. Matlab m-Files for Use in DSP Communication/Configuration

file	location on PC	description
m-files		
runTarget.m	c:\MatlabR12\toolbox\PSI	main routine for running an application on the DSP board
genRTStructure.m		builds the real-time (RT) structure used to download an application to the DSP board
initTarget.m		routine that initializes communications with and downloads the application to the DSP board
RTConfigInitialize.m		routine that configures the 'real-time' info: sample rate, active A/D and D/A channels, etc.
RTConfigDisplay.m		routine that displays 'real-time' configuration to Matlab workspace (as read back from DSP board)
TransConfigInitialize.m		routine that configures the 'transfer' info: shared memory location, size
TransConfigDisplay.m		routine that displays 'transfer' configuration to Matlab workspace (as read back from DSP board)
DebugDisplay.m		reads and displays status memory from 'shared' memory area
support files		
IIboardXControl1.ocx	c:\M6x\DspComp\ActiveX	ActiveX control for communicating with M67 DSP board

Two main DSP C-code applications were developed on this project: One for simply acquiring and storing data from the DSP on the host, and the other for implementing the adaptive control algorithm. A description of the DSP C-code software files is given below in Table 5. All of the DSP code was developed using Texas Instruments Code Composer (Version 2.0).

Table 5. C-Code Software Files for Use on the DSP

file	location on PC	description
Data Acquisition Application		
dataAcq.pjt	c:\projects\dataAcq	Code Composer project file
dataAcq.c		main routine for implementing DSP data acquisition routine
Adaptive Control Application		
adapt1.pjt	c:\projects\adapt-M6x code	Code Composer project file
adaptMain.c		main routine for implementing DSP adaptive control algorithm
adapt_TI.c		transferring and implementing adaptive routines
observer_TI.c		transferring and implementing observer/controller
probe_TI.c		transferring and implementing probe signal
comb_TI.c		transferring and implementing comb filter
realbuf_TI.c		routines for capturing stream of data
plant.c		example plant model
Support Files and Libraries		
matm.c,.lib	c:\C Libraries	misc. matrix and vector operations
hosttalk.c, .lib	c:\C Libraries	higher level routines for processing commands, and transferring data
MIMOState_Space .c, .lib	c:\C Libraries	routines for implementing a MIMO state space controller
realtime_M6x.c, .lib	c:\C Libraries	routines that set-up and support data acquisition on Servo16 and A4D4 I/O modules
transfer.c, .lib	c:\C Libraries	routines for transfer data to/from host PC
generic.cmd	c:\M6x	memory map file

3.5. Control Demonstration Description and Results

A colored random noise cancellation demonstration was performed in PSI's laboratory space to demonstrate the operation of the algorithm. The basic control setup was as shown in Figure 32 below.

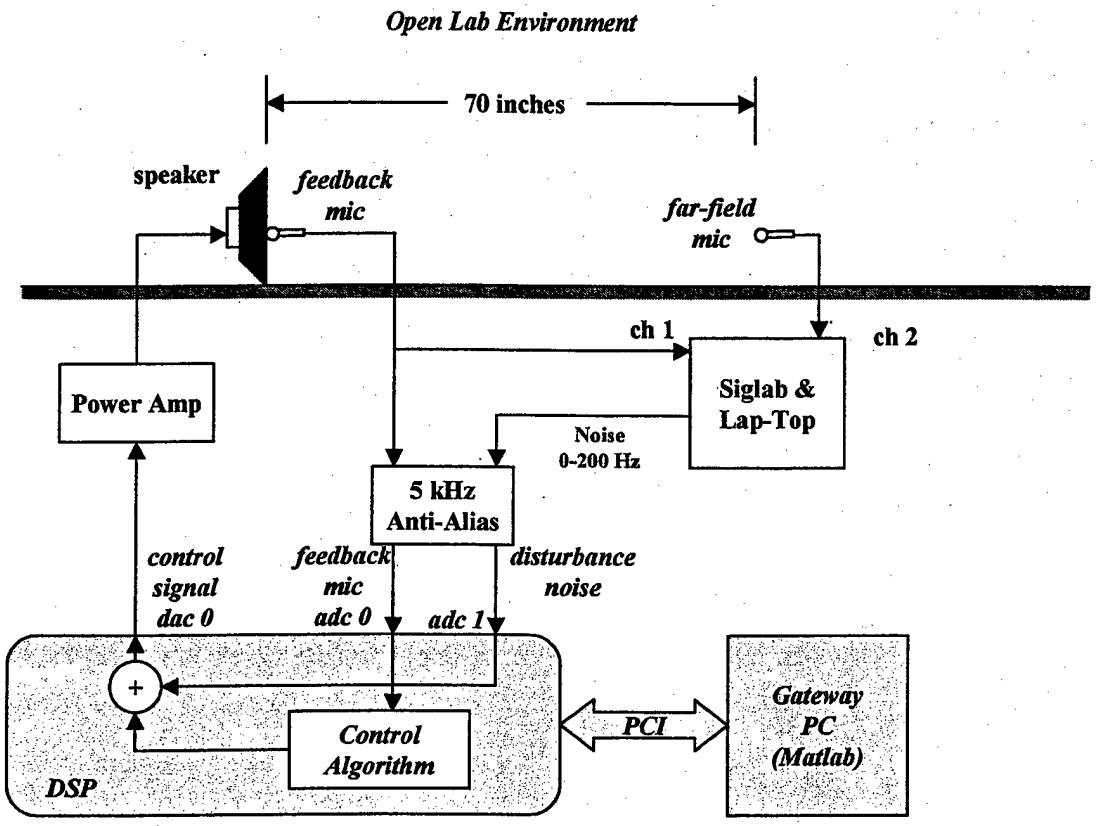

Figure 32. Layout of the Cancellation Experiment

A speaker was used as a disturbance and cancellation source for a random noise cancellation experiment. Sound was measured by means of a nearby microphone (used for feedback cancellation), and performance was monitored approximately 70 inches away by a second microphone. The environment was an open laboratory with a nearby wall, door, workbenches, etc.. The floor was carpeted.

The noise source was generated by a Siglab 2-channel analyzer connected to a lap-top computer running Matlab. Both microphones were monitored at the Siglab. The noise was random between 0-200 Hz with an internal high-order low-pass filter. Both the feedback microphone signal and the noise were fed to the control DSP, which used only

the microphone signal for control adaptation. The noise was simply added to the control signal drive.

A variety of sample rates were used for experimentation in the DSP, with the most successful experiments run at the highest rate (14 kHz). The results of such an experiment, with an observer of 40 states maximum, are shown below in Figure 33. Approximately 10 dB of attenuation was achieved over the significant 100-200 Hz band. While experimentation showed that multi-path and 3-D transmission effects were significant, performance was almost certainly limited chiefly by time-delays through the drive amplifier, processor, and speaker.

Convergence was quite rapid (a few time-windows of 4096 points of data at 14 kHz) for the observer model. Controller design was the limiting factor, because a slow loop was used for gradually increasing the controller authority (this can be modified, but was not, due to time constraints).

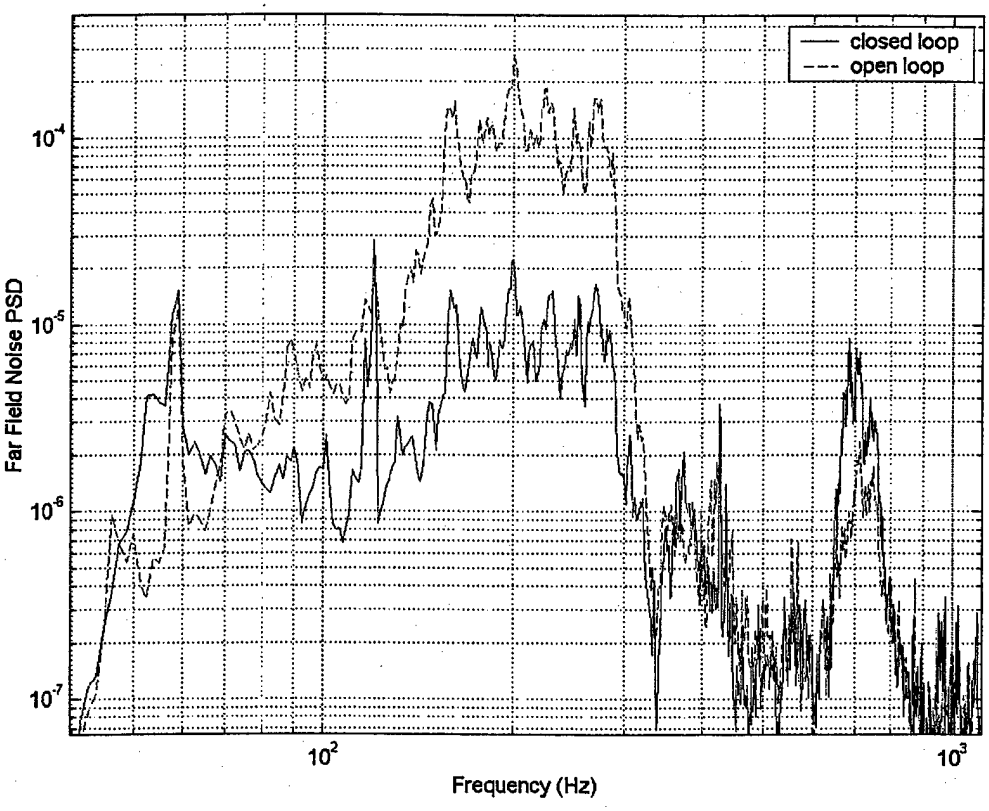

Figure 33. Far-Field Cancellation Results Using Adaptive Algorithm

It was necessary artificially to increase the measurement noise parameter identified by the system prior to use in adaptive design to ensure that the resulting controller was internally stable. As is common with LQG, too high a control effort under low-noise conditions tends to cause the controller to be very aggressive, introducing unstable poles that, while ostensibly closed-loop stable when connected to the system, make the controller extremely sensitive to modeling inaccuracies. Overall, the performance seemed close to the physical limits of the laboratory setup, which seemed dominated by the lags and time delays, as mentioned previously.

4. PULSE MICROJET ACTUATOR

High frequency forcing was one of the numerous concepts that was proposed for reducing high-speed jet noise. The goal of the technique is to affect the far-field jet noise radiation by affecting the airflow before it exits the nozzle. In this case, high-pressure microjets were employed to affect the airflow upstream of the nozzle exit. The microjets were operated at high frequencies (2 kHz) in order to provide an unsteady disturbance to the airflow.

Prior to conducting any experiments, it was necessary to design and fabricate a nozzle that would allow for the microjet injection into the airflow upstream of the nozzle exit. A picture of the nozzle that was used for the experiment is shown in Figure 34. The converging nozzle has an exit diameter of 50.8 mm. The nozzle had four ports for microjet injection and it also had four pressure ports before and after the microjets. This allowed us to measure the static pressure before and after the microjet injection so that we could determine changes brought about by the microjet injection on the airflow. The nozzle was constructed of Nistele 230, a nickel-based material that allowed us to operate the jet at high stagnation temperatures without any active cooling.

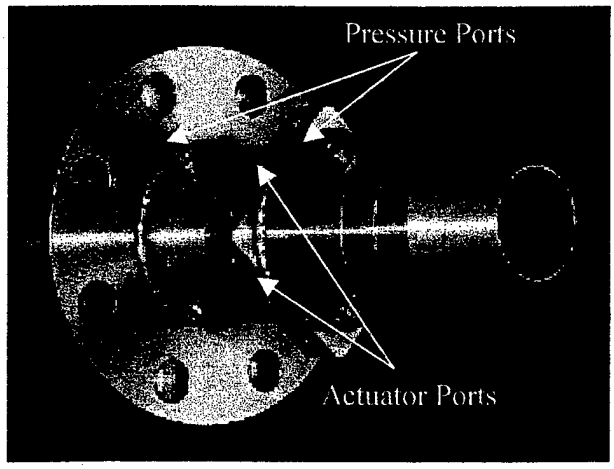

Figure 34. Nozzle for High Frequency Forcing Experiments.

It was also necessary to procure a valve that could handle high pressures and operate at frequencies up to 2 kHz without any active cooling. Such a valve was not found to be commercially available. Therefore, Planning Systems Incorporated (PSI) was contracted

to develop and provide a reasonably priced high-speed valve that could handle the high pressures. The intent was to then purchase 4 of these valves for use on the four ports on the nozzle discussed above. A picture of the valve that was provided to us at the end of the contract is found in Figure 35. This valve was expensive, difficult to operate and it required active cooling. As a result, a new high-speed valve was developed to meet the requirements at FMRL (Fluid Mechanics Research Laboratory). A schematic of the valve

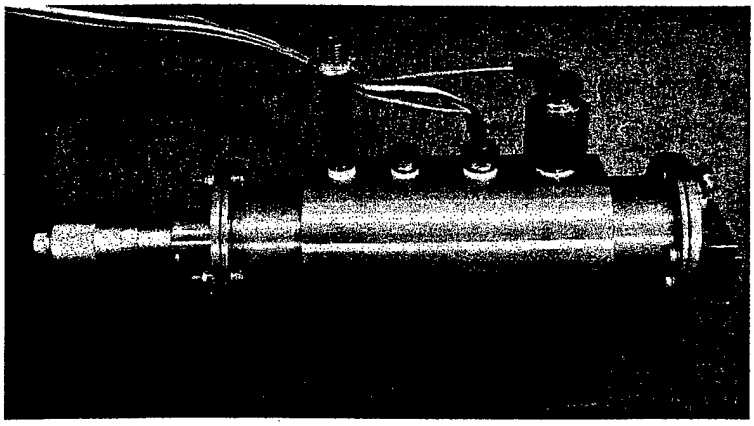

Figure 35. High-speed valve developed by PSI

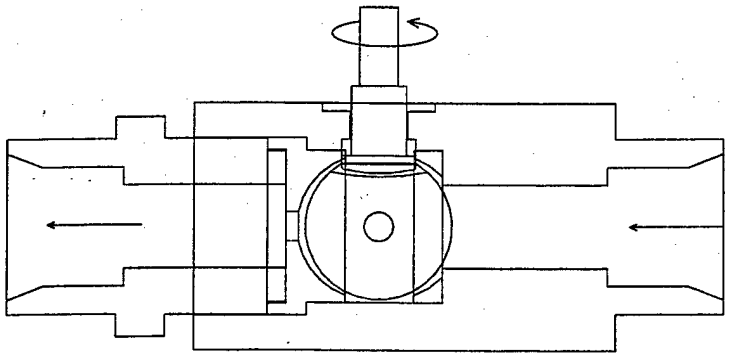

Figure 36. Simple schematic of the high-speed valve developed at FMRL.

Is shown in Figure 36. This valve easily met all of the stated requirements. The only drawback was that it required a high torque motor in order to operate at high pressures. Preliminary results obtained for the valve can be found in Figure 36 and 37. Figure 36 is

the pressure-time plot for the valve output when 500 psi is applied to the valve. The pressure was measured at a distance of 5 diameters downstream of the valve exit. The mean pressure at this point is 42.5 psi with fluctuations of 17.5 psi. Figure 37 is the corresponding narrowband frequency spectrum. As can be seen, the valve is operating well above the required 2 kHz. The other noise peaks in the plot, except for the harmonic at 4.5 kHz, are believed to be a result of the high torque motor. Increasing or decreasing the pressure applied to it could change the operational speed of the valve. An increase in pressure caused the valve to slow down and decrease in pressure caused it to speed up.

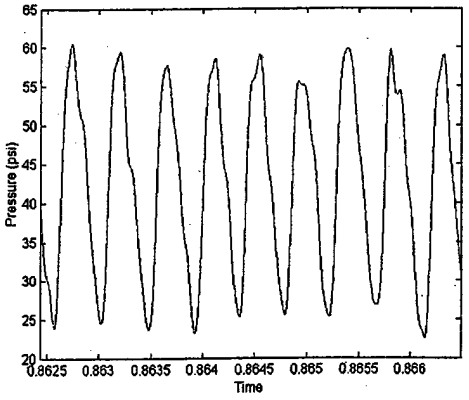

Figure 36. Pressure-time plot for the high-speed valve operated at 500 psi

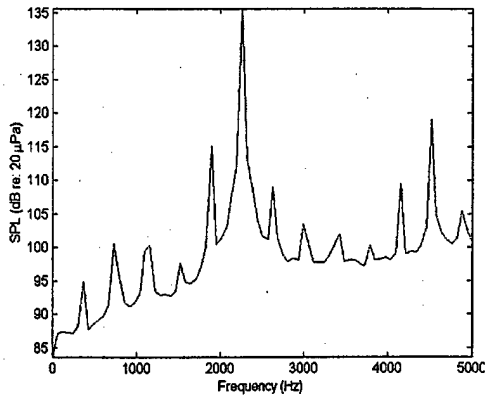

Figure 37. Narrowband frequency spectra corresponding to Figure 36.

Once the nozzle and the valve were completed it was possible to conduct the experiment investigating the effects of high frequency forcing. A picture of the setup for this experiment can be found in Figure 38. The high-speed valve was used to supply all four of the microjets on the nozzle. The microjets were operated at 2.2 kHz and a stagnation pressure of 500 psi. The main jet was operated at a stagnation pressure of 44 psi and a stagnation temperature of 1033 K. The far-field noise radiation was acquired through the use of 8 Bruel & Kjaer 4939 microphones. These microphones were set up at a distance of 65 nozzle diameters in a polar array that varied from 90 to 145 degrees, relative to the upstream jet axis. The far-field noise was measured with and without the microjet injection. As can be seen in Figure 39, there was little or no effect caused by the

microjet injection. In fact, there was even a slight increase in the overall sound pressure level (OASPL) at both 140 and 145 degrees.

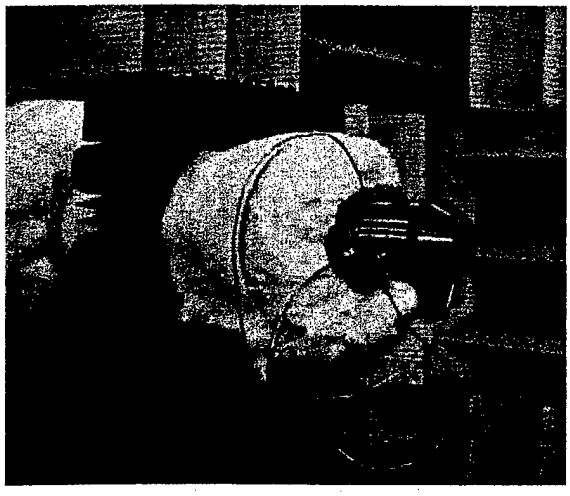

Figure 38. Setup for the high frequency forcing experimental setup.

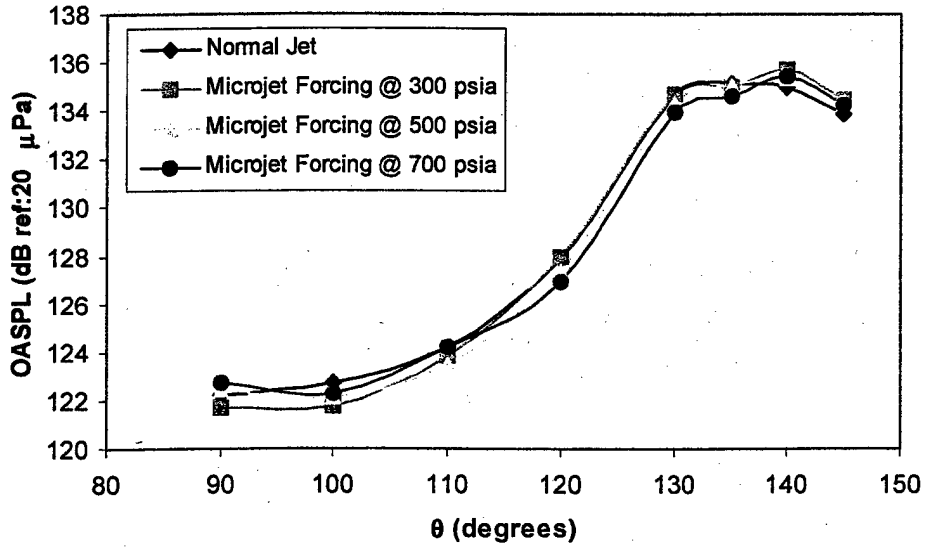

Figure 39. Plot of the far-field noise radiation for the high frequency forcing experiment.

Even though the results suggest that high frequency forcing did not produce any favorable results, we cannot state with certainty that this is the case. There are a number of parameters that can still be investigated, such as the size and number of microjets in

the nozzle. It would also be beneficial to supply each microjet with its own high-speed valve that is close to the nozzle. This would allow for individual control of each of the microjets, as well as reducing the losses that undoubtedly occurred in the setup used for this experiment. Work is currently ongoing at FMRL to develop a smaller high-speed valve that can be used for these types of applications.

5. SUMMARY

A novel high-speed jet noise suppression technique using high-pressure gas microjet injection at the nozzle exit was developed with promising results using the laboratory scale jet. The main jet parameters, the nozzle pressure ratio and the temperature ratio are chosen to correspond with realistic engine operating conditions. Keeping in mind the applicability of the technique to full-scale engines, the microjet mass flow was kept at less than 2% of the primary jet mass flow.

One of the dominant sources of noise from a high-speed jet is intimately related to the large-scale vortical structures that convect at supersonic speeds relative to the ambient medium. The dominant noise from this source consists of two parts: the Mach wave radiation and a contribution due to the unsteady flow associated with eddying motions whose scale is commensurate with the local shear layer thickness. The noise radiation is most intense in the direction given by a uniquely defined convective Mach number due to Oertel[5]. The Mach wave radiation that is quite distinguishable is characterized by strong narrow pressure transients in the far-field microphone signal, referred to as 'crackle', first brought to notice by Ffowcs Williams[8]. It is quantified by the skewness factor of the pressure time signal that does not depend on the scale of the jet. The microjet injection scheme used here significantly reduces its level resulting in about 1.5 dB reduction in the far field OASPL. Additionally, the microjets interfere with the unsteady vortical flow due to large eddies so as to reduce the mixing noise by about 3 dB. The A-weighted spectra that incorporate the full-scale nozzle diameter show total OASPL reductions of about 6 dBA in the peak radiation angle. The microjets are effective probably because they inhibit the formation of the large eddies, the consequence of basic jet instabilities, which are responsible for the crackle and the low frequency component of the mixing noise. When the jet is imperfectly expanded, the commonly observed screech tones are completely suppressed by the microjet injection.

Another major component of the jet noise is due to chaotic small and intermediate scale turbulence in the jet. Although it is difficult to suppress this noise component, our attempts with water injection using microjets appear to show promise.

An attempt is made during this investigation to develop Active Noise Control methods for cancellation of broadband jet noise. A demonstration of successful control architecture has been accomplished using the colored random noise cancellation. During this investigation, an attempt was also made to develop a high frequency actuator with based Piezo-operated valve to provide flow modulation. The valve although showed some promise failed produce sufficient authority to effect the jet flow upstream of the nozzle exit.

Further investigations were carried out to design and built an actuator using the Hartman resonance tube principle. The resulting output of 158 dB from these actuators was again found to be insufficient to modulate the flow upstream of the nozzle exit. A third actuator based on pulsed microjet appears to be most promising for the current application. A specially designed micro valve operating at high pressures and high frequencies was developed and tested successfully. The valve was able to provide a pulsed jet operating at nozzle exit mean pressure of about 45 psia at 2000 Hz. Preliminary experiments using four pulsed jets injected upstream of the nozzle exit in an open loop control configuration showed very little effect on the far-field noise. However, further experiments are being conducted under a continuation ONR grant to further explore the broadband active noise control of jet noise.

6. ACKNOWLEDGEMENT

We would like to thank Dr. Gabriel D. Roy, the program manager, for his patience, encouragement and continued support of this program. This work would have not been started without the foresight and enthusiasm of the RADM Jay Cohen, whose belief of Active Broadband Noise Control will soon come to fruition. Prof. Vijay Arakeri, a visiting professor from Indian Institute of Science has been immensely helpful in improving our understanding of the high-speed jet noise. This project would have not been carried out without the support of Mr Brent Greska, a Ph.D student, Mr. Tom Joseph, an engineer and technical personnel Mr. Bobby Avant and Mr. Bobby DePriest. We like to thank Mr. Lawrence Davis of PSI who is responsible for the development of the control architecture and its implementation. Also, Dr. Ganesh Raman of Illinois Institute of Technology who helped us in the design and development of the Hartman resonance tube actuator.

7. REFERENCES

1. Crighton, D.G., "Orderly structure as a source of jet exhaust noise: Survey lecture", Structure and Mechanisms of Turbulence II, Edited by H. Fiedler, Lecture Notes in Physics, 76, Springer-Verlag, 1977, pp 154-170.
2. Phillips, O.M., "On the generation of sound by supersonic turbulent shear layers", *J. Fluid Mech.*, **9**, 1960, pp. 1-28.
3. Ffowcs Williams, J.F., and Maidanik, G., "The Mach wave field radiated by supersonic turbulent shear flows", *J. Fluid Mech.*, **21**, 1965, pp. 641-657.
4. Ffowcs Williams, J.E., "On the development of Mach waves radiated by small disturbances", *J. Fluid Mech.*, **22**, 1965, pp. 49-55.
5. Oertel, H and Patz, G. "Wirkung von unterschallmanteln auf die Machwellen in der umgebung von Uberschallstrahlen" ISL Report RT 505/81, Institut Franco-Allemand De Recherches, Saint-Louis, France, 1981.
6. Papamoschou, D., "Mach wave elimination from supersonic jets", *AIAA Journal*, **35**, 1997, pp 1604-1611.
7. Laufer, J., Schlinker, R. and Kaplan, R.E., "Experiments on supersonic jet noise", *AIAA Journal*, **14** (4), 1976, pp. 489-504.
8. Ffowcs Williams, J.E., Simson, J., and Virchis, V.J., "Crackle: an annoying component of jet noise", *J. Fluid Mechanics*, **71**, 1975, pp 251-271.
9. Oertel, H, Gatau, F., and George, A., "Dynamik der Machwellen in der Umgebung von Uberschallstrahlen" ISL Report R 124/81, Institut Franco-Allemand De Recherches, Saint-Louis, France, 1981.
10. Krothapalli, A., Venkatakrishnan, and Lourenco, L., "Crackle: A dominant component of supersonic jet mixing noise, *AIAA Paper # 2000-2024*, 6th AIAA/CEAS Aeroacoustics Conference, Hawaii, June 2000.
11. Tam, C.K.W., Golebiowski, M., and Seiner, J.M., "On the two components of turbulent mixing noise from supersonic jets", *AIAA Paper # 96-1176*, May 1996.
12. Tam, C.K.W., "Jet noise: Since 1952", *Theo. and Comp. Fluid Dynamics*, **10**, 1998, pp 393-406.

13. Arakeri, V.H., Krothapalli, A., Siddavram, V., Alkislar, M. and Lourenco, L., "On the use of microjets to suppress turbulence in a Mach 0.9 axisymmetric jet", submitted to *J. Fluid Mechanics,* April 2002.

14. Blackstock, D.T., Fundamentals of Physical Acoustics, *John Wiley & Sons Inc.*, 2000.

15. Papamoschou, D., and Hubbard, D.G., "Visual observations of supersonic transverse jets", *Experiments in Fluids*, **14**, 1993, 468-476.

16. Krothapalli, A., and Strykowski, P.J., "Revisiting screech tones: Effects of temperature", *AIAA Paper # 96-0644*, January 1996.

17. Tanna, H.K., Dean, P.D., and Burrin, R.H., " The generation and radiation of supersonic jet noise", AFAPL-TR-76-65-Vol III, Air Force Aero-Propulsion Laboratory, Wright-Patterson Air Force Base, September 1976.

18. Krothapalli, A., Venkatakrishnan, L., Elavarasan, R., and Lourenco, L., "Turbulence and Noise Suppression of a Supersonic Jet by Water Injection", submitted to *J. Fluid Mechanics,* February 2002.

19. Laufer, J., Kaplan, R.E. and Chu, W.T., "Acoustic modeling of the jet noise abatement problem", *Proceedings of the interagency symposium in transportation noise,* 1973, Stanford University, Stanford, CA.

20. Simonich, J. C., Narayanan, S., Barber, T. J. and Nishimura, M. "Aeroacoustic characterization, noise reduction, and dimensional scaling effects of high subsonic jets", *AIAA Journal*, **39**, 2001, pp. 2062-2069.

21. Blondel, L. A., and Elliott, S. J., "Electropneumatic Transducers as Secondary Actuators for Active Noise Control, Part I: Theoretical Analysis," *J. of Sound and Vib.*, Vol. 219, No. 3, pp. 405-427, Academic Press, 1999.

22. Larimore, W. E., "Canonical Variate Analysis in Identification, Filtering, and Adaptive Control," *Proc. 29th IEEE Conf. on Decision & Control*, HS Rao & T. Dorato, Eds., pp. 445-451, IEEE, New York, 1990.

23. Larimore, W. E., "System Identification of Feedback and 'Causality' Structure Using Canonical Variate Analysis," *Proc. IFAC System Identification Conference '97*, July 1997.

24. Larimore, W. E., "Canonical Variate Analysis in Control and Signal Processing," *Statistical Methods in Control and Signal Processing*, T. Katayama & S. Sugimoto, Eds., Marcel Dekker, New York., 1997.
25. Akaike, H, "A New Look at the Statistical Model Identification," *IEEE Trans. Auto. Control*, Vol. AC-19, No. 6, pp. 716-723, December, 1974.
26. Hurvitch, C. M., and Tsai, C.-L., "Regression and Time Series Model Selection in Small Samples," *Biometrika*, Vol. 76, No. 2, pp. 297-307, 1989.
27. Davis, L. D., "Akaike Information Criterion and Least Squares," Internal PSI Memo, June, 2001.
28. Larimore, W. E., "Order-Recursive Factorization of the Pseudo-Inverse of a Covariance Matrix," *IEEE Trans. Auto. Control*, Vol. 35, No. 12, pp. 1299-1303, December, 1990.
29. Candy, J. V., Bullock, T. E., and Warren, M. E., "Invariant System Description of the Stochastic Realization," *Automatica*, Vol. 15, pp. 493-495, 1979.
30 Kwakernaak, H., and Sivan, R., *Linear Optimal Control Systems*, pp. 536-547, John Wiley and Sons, New York, 1972.
31. Bernstein, D. S., Davis, L. D., and Hyland, D. C., "The Optimal Projection Equations for Reduced-Order, Discrete-Time Modeling, Estimation, and Control," *AIAA J. Guid. Contr. Dyn.*, Vol. 9, pp. 288-293, 1986.